Masterarbeit

Zur Erlangung des akademischen Grades Master

Hybrid functionals in real-time time-dependend density functional theory: implementation in the `exciting` package

Antonio Cillis

Erste Gutachterin: Prof. Dr. Claudia Draxl

Zweite Gutachterin: Prof. Dr. Caterina Cocchi

Eingereicht am Institut für Physik der Humboldt-Universität zu Berlin am: 24.02.2023

Contents

List of Figures

List of Tables

1 Introduction

Electronic-structure codes, like `exciting`, seek to predict properties of crystals, atoms, and molecules. These properties are governed by the complex interactions of the electrons and nuclei that is described by the many-body Schrödinger equation. A widely used method in solid state physics and theoretical chemistry to predict properties on the basis of this complex behavior is density-functional theory (DFT). It has proven to be a powerful tool to predict ground state (GS) related properties of solids and molecules, such as: ground-state energies, electronic densities, equilibrium geometries, bond lengths and angles, lattice constants, forces, elastic constants, and magnetic moments. In practice, within DFT, an approximation is made for the exchange-correlation functional. A popular choice are (semi-)local functionals. However, there are some properties which can not be described with (semi-)local functionals. For these, hybrid functionals can be used, which include a non-local exchange potential. The approximation for the functional not only impacts GS properties, but also of the excited state. To calculate excited-state properties, GS DFT can be extended in the time-dependent regime as time-dependent density functional theory (TDDFT). TDDFT is able to predict excited-state properties such as: transition energies, absorption/emission spectra, and excitonic behavior. Both real-time time-dependent density functional theory (RT-TDDFT) with (semi-)local functionals and hybrids for the ground state were already available in `exciting` [1, 2]. This work consists of the combination of RT-TDDFT and hybrid functionals.

The work is divided into three main sections. In the first section, the theory of hybrid functionals and RT-TDDFT is presented. This includes an introduction to density functional theory and a short discussion about exchange-correlation functionals. Then RT-TDDFT is described. In the second section, the implementation of hybrids in RT-TDDFT in the `exciting` code is described. In the third section, the implementation is applied to diamond and boron nitride. Furthermore, a comparison of the current response and excited electrons between `exciting` and the octopus code is provided for both materials.

2 Theoretical background

2.1 Density functional theory

The many-body problem treated in DFT consists of a system of N electrons which are governed by the Schrödinger equation:

$$\hat{\mathrm{H}}(\{\boldsymbol{r}\})\Psi(\{\boldsymbol{r}\}) = \left(\hat{\mathrm{T}}_{\mathrm{e}}(\{\boldsymbol{r}\}) + \hat{\mathrm{V}}_{\mathrm{e}}(\{\boldsymbol{r}\}) + \hat{\mathrm{V}}_{\mathrm{ext}}\right)\Psi(\{\boldsymbol{r}\}) = E\Psi(\{\boldsymbol{r}\}), \tag{2.1}$$

where $\hat{\mathrm{T}}_{\mathrm{e}}$ stands for the electronic kinetic energy operator, $\hat{\mathrm{V}}_{\mathrm{e}}$ for the operator of the Coulomb energy between electrons and $\hat{\mathrm{V}}_{\mathrm{ext}}$ for the operator of the Coulomb energy of electrons with the nuclei. $\hat{\mathrm{T}}_{\mathrm{e}}$ and $\hat{\mathrm{V}}_{\mathrm{e}}$ are universally defined, i.e. they take the same form for any many-body problem. The external potential $\hat{\mathrm{V}}_{\mathrm{ext}}$ uniquely defines the Hamiltonian of the many-body problem.

The proposal of DFT dates back to Hohenberg and Kohn's seminal paper of 1964 [3]. They formulated a one-to-one correspondence between the GS density $n_0(\boldsymbol{r})$ and the external potential $\hat{\mathrm{V}}_{\mathrm{ext}}$ of a many-body system [3]. If only $n_0(\boldsymbol{r})$ is known, the $\hat{\mathrm{V}}_{\mathrm{ext}}$ that produced this density can in principle be obtained. With $\hat{\mathrm{V}}_{\mathrm{ext}}$, the Hamiltonian can be constructed, which gives access to all eigenstates and eigenvalues of the system. The conclusion is that the many-body problem can, in principle, be formulated in terms of $n_0(\boldsymbol{r})$. Thus, the Hohenberg Kohn theorem represents the ability to formulate the many-body problems in terms of the density as a fundamental variable, which depends on three spatial variables, in contrast to the 3N spatial coordinates of the wave function (WF) Ψ. Additionally, Hohenberg and Kohn established a variational principle in terms of the density [3]: The global minimum of the energy functional $E[n]$ should only be produced by $n_0(\boldsymbol{r})$.

A difficulty is that the formulation of the energy as an explicit functional of the electron density is generally not known. To circumvent this difficulty, Kohn and Sham proposed the use of independent electrons as an auxiliary system, which reproduces the GS electron density of the interacting system [4]. The independent electrons of the Kohn-Sham (KS) system are described by a set of one particle wave functions $\{\psi_{n\boldsymbol{k}}(\boldsymbol{r}))\}$ in a periodic potential with a set of k points $\boldsymbol{k}$ and band indexes n. An advantage of this system of independent electrons is that it has a simple construction of $n(\boldsymbol{r})$:

$$n(\boldsymbol{r}) = N \int d\boldsymbol{r}_2 d\boldsymbol{r}_3 d \ldots \boldsymbol{r}_N |\Psi(\boldsymbol{r}, \boldsymbol{r}_2, \boldsymbol{r}_3, \ldots \boldsymbol{r}_N)|^2 \xrightarrow{\{\psi_{n\boldsymbol{k}}(\boldsymbol{r})\}} \sum_{n\boldsymbol{k}}^{N} |\psi_{n\boldsymbol{k}}(\boldsymbol{r}))|^2. \tag{2.2}$$

The KS system is then described by effective one-particle Schrödinger equations [5]:

$$\left[\hat{\mathrm{t}}_{\mathrm{e}}(\boldsymbol{r}) + \hat{\upsilon}_{\mathrm{KS}}(\boldsymbol{r})\right] \psi_{n\boldsymbol{k}}(\boldsymbol{r}) = \epsilon_{n\boldsymbol{k}} \psi_{n\boldsymbol{k}}(\boldsymbol{r}), \tag{2.3}$$

with the effective potential:

$$\hat{\upsilon}_{\mathrm{KS}} = \hat{\upsilon}_{\mathrm{ext}} + \hat{\upsilon}_{\mathrm{H}} + \hat{\upsilon}_{\mathrm{XC}}. \tag{2.4}$$

The first term, $\hat{\upsilon}_{\mathrm{ext}}$, describes the interaction between electrons and nuclei:

$$\hat{\upsilon}_{\mathrm{ext}}(\boldsymbol{r}) = -\sum_{j=1}^{N_{\mathrm{n}}} \frac{\mathrm{Z}_j}{|\boldsymbol{r} - \boldsymbol{R}_j|}. \tag{2.5}$$

N_{n} denotes the number of nuclei, Z_j the nuclear charge, and $\boldsymbol{R}_j$ the position of the j-th nucleus. The second term, $\hat{\upsilon}_{\mathrm{H}}$, is the Hartree potential, which represents the interactions between electrons as understood in a classic electrostatic picture:

$$\hat{\upsilon}_{\mathrm{H}}(\boldsymbol{r}) = \int \frac{n(\boldsymbol{r})}{|\boldsymbol{r} - \boldsymbol{r}'|} d\boldsymbol{r}'. \tag{2.6}$$

The third term $\hat{\upsilon}_{\mathrm{XC}}$ is the exchange-correlation (XC), which embodies the quantum-mechanical part of the electron-electron interaction. While the energy eigenvalues and wave functions of this KS system should not be misinterpreted as reproducing a real physical system[1], its GS electron density is in principle exact [6]. The use of the density as a fundamental variable and the formulation of the KS system form the basis of modern DFT [5].

DFT is an exact theory. However, the unknown form of the energy functional $E[n]$ has been shifted to the unknown form of $\hat{\upsilon}_{\mathrm{XC}}$. In practice, several approximations have been devoped for this term [6]. The choice of approximation determines the accuracy and computational cost. The most important approximations used in this work are discussed in the next section. When $\hat{\upsilon}_{\mathrm{XC}}$ is known, the KS equations can be solved. They must be solved self-consistently, since the effective potential $\hat{\upsilon}_{\mathrm{KS}}$ is in itself a functional of $n(\boldsymbol{r})$. The way to solve a many-body problem by means of DFT would be:

---

[1] except for the highest occupied orbital which represents the ionization energy

1. Make an initial guess for $n(\boldsymbol{r})$
2. Construct $\hat{\upsilon}_{\mathrm{KS}}$ from $n(\boldsymbol{r})$
3. Solve the KS equations obtaining the KS wave functions $\{\psi_{n\boldsymbol{k}}(\boldsymbol{r}))\}$
4. Construct $n(\boldsymbol{r})$ from the calculated $\{\psi_{n\boldsymbol{k}}(\boldsymbol{r}))\}$ (Eq. 2.2)
5. Go back to step 2 until a convergence target is reached
6. Obtain the quantities of interest from $\{\psi_{n\boldsymbol{k}}(\boldsymbol{r}))\}$

2.1.1 Functionals for exchange and correlation

Many approximations for $\hat{\upsilon}_{\mathrm{XC}}$ have been developed and more than of 250 have been proposed in the last 25 years [7]. Two classes of these functionals, which will be highlighted here, are (semi-)local functionals and hybrid functionals. Traditionally, the unknown functional $\hat{\upsilon}_{\mathrm{XC}}$ is split into an exchange and a correlation part. Both of these parts lower the total energy of the system ($E_{\mathrm{X}} < 0$ and $E_{\mathrm{C}} \leq 0$), where the exchange energy often dominates over the correlation energy [8]. In other words, they lower the probability of one electron finding another electron in its vicinity.

The exchange energy E_{X} describes the Coulomb energy two electrons contribute due to the Pauli exclusion principle: Two electrons, which share a quantum-mechanical state, spatially avoid each other. The exchange energy can be defined with KS wave functions as:

$$E_{\mathrm{X}} = -\frac{1}{2}\sum_{n,n'}^{\text{occ.}}\sum_{\boldsymbol{k},\boldsymbol{k}'}^{\text{BZ}}\int \frac{\psi^{*}_{n\boldsymbol{k}}(\boldsymbol{r})\psi^{*}_{n'\boldsymbol{k}'}(\boldsymbol{r}')\psi_{n'\boldsymbol{k}'}(\boldsymbol{r})\psi_{n\boldsymbol{k}}(\boldsymbol{r}')}{|\boldsymbol{r}-\boldsymbol{r}'|} d\boldsymbol{r}d\boldsymbol{r}', \tag{2.7}$$

where $\boldsymbol{k}$ and $\boldsymbol{k}'$ stand for the Bloch vectors and n and n' stand for the band indices. The sum over the KS states in Eq. 2.7 includes nonphysical self interaction energies ($n = n'$). The reason for this is that it is customary to define the Hartree potential (Eq. 2.6) in terms of the total electron density. In this way, it includes the interaction of an electron with the density created from all electrons, including itself. In the sum of both energies, the self interaction error of the Hartree energy cancels with the self interaction of the exchange energy. However, when E_{XC} is approximated, the self interaction error must be factored in for considerations about its accuracy.

The correlation energy E_C can be defined as the difference between the full energy functional $\langle\Psi|\,\hat{\mathrm{H}}\,|\Psi\rangle$ and the energy functional constructed from statistically independent KS WFs, which react to each other's mean field. However, electrons coordinate their movement in order to minimize their Coulomb energy. All energy contributions which come from the correlated movements between electrons are included in E_C.

2.1.2 Local and semi-local functionals

A first approximation would be to take the functional of a simple many-body system and insert it into the given many-body problem. The local density approximation (LDA) takes the exchange-correlation energy of the homogeneous electron gas and employs it locally [4]. It is given by:

$$E_\mathrm{LDA}[n] = \int n(\boldsymbol{r})e_\mathrm{xc}^\mathrm{Jellium}(\boldsymbol{r}, n(\boldsymbol{r}))d\boldsymbol{r}. \tag{2.8}$$

This approximation might seem crude, but yields physically meaningful results. Lattice constants, for example, can be predicted within a few percent with LDA [9]. One explanation is that LDA adheres to the sum rules of the exchange functional [9]. With an arbitrary approximation, these inherent sum rules might be difficult to reproduce.

The generalized gradient approximation (GGA) seeks to improve upon the local dependence of LDA. It introduces an additional dependence on the magnitude of the gradient of the density. In order to preserve the sum rules, Eq. 2.8 can be modified by a dimensionless function F:

$$E_{GGA}[n] = \int n(\boldsymbol{r})e_\mathrm{xc}(\boldsymbol{r}, n(\boldsymbol{r}), |\nabla n(\boldsymbol{r})|)d\boldsymbol{r} = \int n(\boldsymbol{r})e_\mathrm{xc}^\mathrm{Jellium}(\boldsymbol{r}, n(\boldsymbol{r}))F(n(\boldsymbol{r}), |\nabla n(\boldsymbol{r})|)d\boldsymbol{r}. \tag{2.9}$$

One of the most popular GGA functionals is PBE [10]. GGA can give results closer to experiments than LDA, for example lattice parameters. However, while local and semi-local functionals can reproduce ground state properties, they fail to accurately predict excited-state properties.

2.1.3 Theory of band gaps

One problem with (semi-)local functionals is the insufficient description of excitation energies, for example the band gap when it is calculated as a difference between KS energies.

Borlido et al. benchmarked the band gap for 12 functionals across a set of 472 nonmagnetic materials [11]. They found that band gaps were underestimated roughly by 50% with LDA and 40% with PBE [11]. Furthermore, around 7% of the tested materials where erroneously predicted with a band gap smaller than 0.01 eV [11]. This trend was most pronounced with transition metal compounds [11]. This underestimation is consistent over the k path.

The difference between ionization energy I and electron affinity A constitutes a fundamental band gap ϵ_{g}. The "band gap problem" arises from the fact that the fundamental gap is different from the KS band gap, defined as the difference between the highest occupied and lowest unoccupied KS eigenvalues $\epsilon_{\mathrm{g}}^{\mathrm{KS}}$. In contrast to the KS band gap, the fundamental gap exhibits a discontinuous (positive) jump Δ_{XC} when an electron is added to a solid:

$$E_{\mathrm{g}}^{\mathrm{F}} = I - A = \epsilon_{\mathrm{N+1}}^{\mathrm{KS}}(\mathrm{N}) - \epsilon_{\mathrm{N}}^{\mathrm{KS}}(\mathrm{N}) + \epsilon_{\mathrm{N+1}}^{\mathrm{KS}}(\mathrm{N}+1) - \epsilon_{\mathrm{N+1}}^{\mathrm{KS}}(\mathrm{N}) = \epsilon_{\mathrm{g}}^{\mathrm{KS}} + \Delta_{\mathrm{XS}}, \tag{2.10}$$

where $\epsilon_{\mathrm{N}}^{\mathrm{KS}}(\mathrm{M})$ denotes the N-th KS eigenvalue of the M electron system. Hence, a discrepancy is expected between the KS band gap and the fundamental gap. Local and semi local functionals show no discontinuity with respect to the fractional charge difference ($\Delta_{\mathrm{XS}} = 0$) [12]. These functionals tend to over-delocalize the states. This delocalization may be driven by the fact that the (semi-)local functionals do not cancel the self-interaction error [13]. They fall off exponentially and thus do not represent the asymptotic behavior of the real XC functional:

$$\upsilon_{\mathrm{XC}} \longrightarrow \frac{1}{r} \quad \text{for} \quad r \longrightarrow \infty. \tag{2.11}$$

Contrarily, the Hartree Fock (HF) method tends to overestimate band gaps, often by more than 50% [8]. For example, HF has been shown to predict Germanium as an insulator [14]. The overestimation even goes as far as predicting a small gap semiconductor for the homogeneous electron gas [15]. This intrinsic failure to predict small-gap and no-gap solids stems from the absent electron correlation [16]. Collectively, the correlation would reduce the repulsive interaction between two electrons. This electron "screening" is missing from the HF picture, overly localizing the states.

2.1.4 Hybrid functionals

Hybrid functionals take an “best of both worlds” approach: They mix the density-dependent semi-local functionals and the exact HF exchange. Thus, a degree of error cancellation can be taken advantage of and the self interaction error can be partially compensated. The basic idea of hybrid functionals is to replace a fraction of the local or semi local exchange with the non-local HF-like exchange (Eq. 2.7):

$$\mathrm{E}_{\mathrm{XC}}^{\mathrm{Hyb}} = \mathrm{E}_{\mathrm{C}}^{\mathrm{L}} + (1-\alpha)\mathrm{E}_{\mathrm{X}}^{\mathrm{L}} + \alpha\mathrm{E}_{\mathrm{X}}^{\mathrm{NL}}, \tag{2.12}$$

with α as a mixing parameter between zero and one. Consequently, the same fraction of the local exchange potential $\hat{\upsilon}_{\mathrm{X}}^{\mathrm{L}}$ is replaced by the non-local exchange potential $\hat{\upsilon}_{\mathrm{X}}^{\mathrm{NL}}$ in the KS equations [12]. The derivative of the corresponding exchange-correlation potential $\hat{\upsilon}_{\mathrm{X}}^{\mathrm{NL}} = \frac{\delta E_{\mathrm{X}}[n]}{\delta n(\boldsymbol{r})}$ cannot be taken directly, since only the orbital dependent form of E_{X} is known [12]. Thus, the incorporation of the HF exchange into the KS approach constitutes a step outside the standard KS scheme.

A generalized Kohn Scham (GKS) formalism can be employed to provide this inclusion. Apart from the self interaction correction, this formalism incorporates part of the derivative discontinuity into the KS band gap. This way, the difference of GKS eigenvalues can be used to approximate $E_{\mathrm{g}}^{\mathrm{F}}$ directly [17]. The GKS framework has proven powerful for its ability to predict band gaps. The intricacies of GKS are beyond this work. Only the single particle equations shall be given here [18]:

$$\begin{aligned}\epsilon_{n\boldsymbol{k}}\psi_{n\boldsymbol{k}}(\boldsymbol{r}) = \Big[-\frac{1}{2}\nabla_{\boldsymbol{r}}^2 + \hat{\upsilon}_{\mathrm{ext}}(\boldsymbol{r}) + \hat{\upsilon}_{\mathrm{H}}(\boldsymbol{r}) + \hat{\upsilon}_{\mathrm{C}}^{\mathrm{L}}(\boldsymbol{r}) + (1-\alpha)\hat{\upsilon}_{\mathrm{X}}^{\mathrm{L}}(\boldsymbol{r})\Big]\psi_{n\boldsymbol{k}}(\boldsymbol{r}) \\ + \alpha\int \hat{\upsilon}_{\mathrm{X}}^{\mathrm{NL}}(\boldsymbol{r},\boldsymbol{r}')\psi_{n\boldsymbol{k}}(\boldsymbol{r}')d\boldsymbol{r}',\end{aligned} \tag{2.13}$$

where $\hat{\upsilon}_{\mathrm{X}}^{\mathrm{NL}}$ introduces a direct non-local orbital interdependence to the system [18, 12]:

$$\int \hat{\upsilon}_{\mathrm{X}}^{\mathrm{NL}}(\boldsymbol{r},\boldsymbol{r}')\psi_{n\boldsymbol{k}}(\boldsymbol{r}')d\boldsymbol{r}' = -\sum_{n'}^{\mathrm{occ.}}\sum_{\boldsymbol{k}'}^{\mathrm{BZ}}\int \frac{\psi_{n'\boldsymbol{k}'}(\boldsymbol{r})\big(\psi_{n'\boldsymbol{k}'}(\boldsymbol{r}')\big)^*}{|\boldsymbol{r}-\boldsymbol{r}'|}\psi_{n\boldsymbol{k}}(\boldsymbol{r}')d\boldsymbol{r}'. \tag{2.14}$$

A popular hybrid functional is PBE0, where α is set as 0.25, and PBE is employed as the local functional [19]:

$$\mathrm{E}_{\mathrm{XC}}^{\mathrm{PBE0}} = \mathrm{E}_{\mathrm{C}}^{\mathrm{PBE}} + (1-\alpha)\mathrm{E}_{\mathrm{X}}^{\mathrm{PBE}} + \alpha\mathrm{E}_{\mathrm{X}}^{\mathrm{HF}}. \tag{2.15}$$

PBE0 is considered to be a suitable functional for wide-gap materials due to the non-vanishing long range behavior of the HF exchange [8]. Furthermore, this long range exchange part is needed to describe the bound states below the band gap [8]. Borlido et al. found that PBE0 overestimates the band gap by about 50% [11] . Especially band gaps under 5 eV were overestimated by a huge margin [11].

For small-gap and no-gap materials, the exchange energy should go to zero for distant electron interactions. Since the long-range HF exchange gives unphysical results at the Fermi surface, it must be substituted for large distances [8]. This can be implemented by dividing the exchange energy in a short range (SR) and long range (LR) part [20]. The HSE06 functional uses the error function $\mathrm{erf}(x)$ for the division, with ω as a screening parameter: [20, 21].

$$\frac{1}{r} = \underbrace{\frac{1-\mathrm{erf}(\omega r)}{r}}_{\mathrm{SR}} + \underbrace{\frac{\mathrm{erf}(\omega r)}{r}}_{\mathrm{LR}} . \tag{2.16}$$

The HSE06 functional replaces only the SR part of PBE exchange with that of HF ($\alpha = 0.25$, $\omega = 0.11\frac{1}{\mathrm{a_0}}$) [21]:

$$\mathrm{E}_{\mathrm{XC}}^{\mathrm{HSE06}} = \mathrm{E}_{\mathrm{C}}^{\mathrm{PBE}} + (1-\alpha)\mathrm{E}_{\mathrm{X}}^{\mathrm{PBE,SR}}(\omega) + \alpha\mathrm{E}_{\mathrm{X}}^{\mathrm{HF,SR}}(\omega) + \mathrm{E}_{\mathrm{X}}^{\mathrm{PBE,LR}}(\omega). \tag{2.17}$$

HSE06 goes to PBE at $\omega \to \infty$ and to PBE0 at $\omega \to 0$. Both PBE0 and HSE06 go to PBE for $\alpha \to 0$. Apart from reducing the computational cost, this improves the accuracy for small gap semiconductors. Indeed, Borlido et al. found that HSE06 shows one of the best performances of the considered 12 functionals with a mean percentage error of 9.6% and mean error of -0.1 eV [11]. It exhibits remarkably small errors for *sp* bounded compounds. However, for band gaps over 5 eV, HSE06 tends to underestimate the band gaps.

The choice of parameters characterizing the range and magnitude of the long-range exchange is generally dependent on the material [8]. In recent years, there have been successful approaches which “optimally tune” ω and α from material properties obtained within the calculation [22].

2.2 Time dependent density functional theory

TDDFT is the time-dependent extension of DFT. When the many-body problem of Eq. 2.1 is under the influence of a time-dependent potential, the evolution of the respective wave function is governed by the time-dependent Schrödinger equation:

$$\hat{\mathrm{H}}(\{\boldsymbol{r}\},t)\Psi(\{\boldsymbol{r}\},t) = \Big[\hat{\mathrm{T}}_{\mathrm{e}}(\{\boldsymbol{r}\}) + \hat{\mathrm{V}}_{\mathrm{ee}}(\{\boldsymbol{r}\}) + \hat{\mathrm{V}}_{\mathrm{ext}}(t)\Big]\Psi(\{\boldsymbol{r}\},t) = \mathrm{i}\frac{\partial\Psi(\{\boldsymbol{r}\},t)}{\partial t}, \qquad (2.18)$$

where $\{\boldsymbol{r}\} = \{\boldsymbol{r}_1, \boldsymbol{r}_2 \cdots \boldsymbol{r}_{\mathrm{N}}\}$ represents the spatial coordinates of the N electrons. This equation determines Ψ at any time t, if $\hat{\mathrm{H}}$ and the initial state of the system $\Psi(\{\boldsymbol{r}\}, t = t_0)$ are known. $\hat{\mathrm{V}}_{\mathrm{ext}}(t)$ represents the electron interaction with time-dependent external fields, such as produced by the nuclei or a laser pulse.

In 1984, Runge and Gross formulated a one-to-one correspondence between the external potential $\hat{\mathrm{V}}_{\mathrm{ext}}(t)$ and the electron density $n(t)$ at any time t [23]. They showed that two potentials, which differ by more than a time dependent function $f(t)$, can not produce the same time-dependent density. The Runge-Gross theorem laid the foundation for the construction of time-dependent Kohn Sham equations which, similarly to DFT, mimic the time-dependent electron density $n(t)$ of the interacting system:

$$\Big[-\frac{1}{2}\nabla^2_{\boldsymbol{r}} + \hat{\upsilon}_{\mathrm{ext}}(\boldsymbol{r},t) + \hat{\upsilon}_{\mathrm{H}}(\boldsymbol{r},t) + \hat{\upsilon}_{\mathrm{XC}}(\boldsymbol{r},t)\Big]\psi_{n\boldsymbol{k}}(\boldsymbol{r},t) = \mathrm{i}\frac{\partial\psi_{n\boldsymbol{k}}(\boldsymbol{r},t)}{\partial t}. \qquad (2.19)$$

The time-dependent XC potential represents not only interactions which depend non-locally on space, but also on the initial KS states and initial many-body wave function. There have been attempts to incorporate the initial KS states dependence into the functional [24]. However, in practice the causality of the potential is often avoided. The usual approximation lies in constructing an adiabatic functional, which takes the GS XC functional and evaluates it for $n(t)$ at time t:

$$\hat{\upsilon}^{\mathrm{AD}}_{\mathrm{XC}}(\boldsymbol{r},t) = \hat{\upsilon}^{\mathrm{GS}}_{\mathrm{XC}}(\boldsymbol{r},t)\big|_{n(t)}. \qquad (2.20)$$

A widely used functional is the adiabatic LDA (ALDA). In practice, it can be convenient to tread TDDFT in the frequency rather than the time domain.

Linear response TDDFT. For a set of systems with small time-dependent perturbation, the excitation energies may be obtained in the linear response (LR) regime, where the change in density δn to a change in external KS potential $\delta\upsilon^{\mathrm{KS}}_{\mathrm{ext}}$ is evaluated in frequency space and mediated by the KS linear response function χ^{KS}:

$$\delta n(\boldsymbol{r},\omega) = \int d\boldsymbol{r}'\chi^{\mathrm{KS}}(\boldsymbol{r},\boldsymbol{r}',\omega)\delta\upsilon^{\mathrm{KS}}_{\mathrm{ext}}(\boldsymbol{r}',\omega). \qquad (2.21)$$

This approximation yields good results for a variety of materials and is convenient to evaluate quantities directly dependent on ω. However, nonlinear effects fall beyond this formalism.

For LR TDDFT, the non-local functionals give improved excitation energies over local functionals [5]. One reason is that the right asymptotic behavior (Eq. 2.11) leads to improved description of unoccupied states. Another reasoning is that for XC funcionals in TDDFT, the evolution in terms of density response δn plays a much bigger role than the minimization of the energy [25]. This can worsen the performance of many (semi-)local DFT functionals, which are designed to approximate integrated properties of the system rather than n itself.

2.2.1 Real time - TDDFT

For a set of problems where the time-depenent response is of interest, the KS equations may be evolved in real time (RT). In practice, the KS states are evolved for small time steps Δt. For this purpose, it is convenient to rewrite the time evolution of the KS states in terms of the linear propagator $\hat{\mathrm{U}}$:

$$\psi_i(t+\Delta t) = \hat{\mathrm{U}}(t, t+\Delta t)\psi_i(t). \tag{2.22}$$

This expression can be written in terms of an exponential:

$$\hat{\mathrm{U}}(t, t+\Delta t) = \hat{\mathrm{T}}\left[\exp\Big(-\mathrm{i}\int_t^{t+\Delta t} \hat{\mathrm{H}}(\tau) d\tau\Big)\right], \tag{2.23}$$

where $\hat{\mathrm{T}}$ represents the ordering of the expression in brackets over the Keldysh pseudotime τ. The choice of time step size and propagator function with which to approximate $\hat{\mathrm{U}}$ represents a balance between computational cost and accuracy. As a rule of thumb, the upper limit of the time step can be chosen such that $\hat{\mathrm{H}}$ can be seen as constant in the given span. The accuracy of the propagator function depends on physical properties of both the material and the applied field [26]. In `exciting`, the following propagators are available [2]:

- Simple exponential
- Exponential at midpoint
- Approximate enforced time-reversal symmetry

- Commutator-Free Magnus expansion of 4th order
- Exponential using a basis of the Hamiltonian eigenvectors
- Runge-Kutta method of 4th order

Time-dependent external field. When the GS is chosen as the initial state of the system, it evolves in RT-TDDFT due to an external perturbation. In this work, an external perturbation which takes the form of an applied electric field $\boldsymbol{E}(\boldsymbol{r},t)$ is considered. Often used is the dipole approximation, so that $\boldsymbol{E}(t)$ can be seen as constant over the unit cell. The electric field introduces a term to the Hamiltonian which shifts the momenta of the particles. The Hamiltonian is given by:

$$\hat{\mathrm{H}}\psi_{n\boldsymbol{k}}(\boldsymbol{r},t) = \left[\frac{1}{2}\Big(\frac{\nabla_{\boldsymbol{r}}}{i} + \frac{\boldsymbol{A}(t)}{c}\Big)^2 + \upsilon_{\mathrm{KS}}(\boldsymbol{r},t)\right]\psi_{n\boldsymbol{k}}(\boldsymbol{r},t) = \mathrm{i}\frac{\partial\psi_{n\boldsymbol{k}}(\boldsymbol{r},t)}{\partial t}, \tag{2.24}$$

where $\boldsymbol{A}(t)$ denotes the vector potential $-c\int_0^t \boldsymbol{E}(t')dT'$. The vector potential itself is given by $\boldsymbol{A}(t) = \boldsymbol{A}_{\mathrm{ext}}(t) + \boldsymbol{A}_{\mathrm{ind}}(t)$. The external vector potential is determined by the displacement field $\boldsymbol{A}_{\mathrm{ext}}(t) = -c\int_0^t \boldsymbol{D}(t')dT'$. The induced vector field is interdependent with the current density via the relation $\frac{d^2\boldsymbol{A}_{\mathrm{ind}}(t)}{dt^2} = 4\pi c\boldsymbol{J}_{\mathrm{ind}}$.

2.2.2 Physical properties

Macroscopic current density. An electric field moves the electrons from their equilibrium positions. This gives rise to an electric current. The macroscopic current density $\boldsymbol{J}_{\mathrm{ind}}$ can be written in terms of a commutator between the Hamiltonian and the position operator:

$$\boldsymbol{J}_{\mathrm{ind}}(t) = \mathrm{Re}(\langle\Psi(t)|\,[\boldsymbol{r},\hat{H}]\,|\Psi(t)\rangle). \tag{2.25}$$

For all local components of the Hamiltonian, $[\boldsymbol{r},\hat{H}]$ is zero. When the KS potential is local, only the commutator with the vector potential and momentum operator give a non-zero contribution. These two terms represent a paramagnetic current density $\boldsymbol{J}_{\mathrm{para}}$ acting with the electric field and a diamagnetic current density $\boldsymbol{J}_{\mathrm{dia}}$ acting against it:

$$\begin{aligned}\boldsymbol{J}_{\mathrm{ind}}(t) &= \frac{\mathrm{i}}{\Omega}\sum_{n\boldsymbol{k}} w_{\boldsymbol{k}} f_{n\boldsymbol{k}}\,\langle\psi_{n\boldsymbol{k}}(t)|\,\hat{\boldsymbol{p}}\,|\psi_{n\boldsymbol{k}}(t)\rangle - \frac{N\boldsymbol{A}(t)}{c\,\Omega} \\ &= \boldsymbol{J}_{\mathrm{para}}(t) + \boldsymbol{J}_{\mathrm{dia}}(t),\end{aligned} \tag{2.26}$$

where Ω is the unit cell volume, $w_{\boldsymbol{k}}$ the weight of $\boldsymbol{k}$, $f_{n\boldsymbol{k}}$ the occupation of the KS state, and N the number of valence electrons. When the KS potential is non-local, like in the case of hybrid functionals, a non-local current is included in Eq. 2.26 which is described in section 3.2.2.

Dielectric tensor and optical conductivity tensor. Optical experiments are often used to measure the electronic properties of solids. The optical conductivity σ governs the relationship between the inducing electric field and the electrical conductivity. In RT-TDDFT, σ can be calculated in terms of the current density as:

$$\sigma_{\alpha\beta}(\omega) = \frac{\boldsymbol{J}_{\alpha}(\omega)}{E_{\beta}(\omega)}, \tag{2.27}$$

where α and β are Cartesian components. The dielectric function ε can be calculated as:

$$\varepsilon_{\alpha\beta}(\omega) = \delta_{\alpha\beta} + \frac{4\pi \mathrm{i}\sigma_{\alpha\beta}(\omega)}{\omega}. \tag{2.28}$$

Number of excited electrons. Another quantity of interest is the number of excited electrons per unit cell $N_{\mathrm{exc}}(t)$. In RT-TDDFT, the WFs of the excited states are not calculated explicitly. When the initial state of the system $\Psi(\{\boldsymbol{r}\}, t = t_0)$ is chosen as the GS, an external perturbation causes the KS functions to project upon previously unoccupied states. The evolved WF can then be projected on the GS to calculate $N_{\mathrm{exc}}(t)$. The projection $m^{\mathrm{e}}_{j\boldsymbol{k}}(t)$ of the evolved KS state $\psi_{\boldsymbol{k}}(t)$ onto the jth GS $\psi_{j\boldsymbol{k}}(0)$ at the k point $\boldsymbol{k}$ can be calculated as [2]:

$$m^{\mathrm{e}}_{j\boldsymbol{k}}(t) = \sum_{n} f_{n\boldsymbol{k}} | \langle \psi_{j\boldsymbol{k}}(0) | \psi_{n\boldsymbol{k}}(t) \rangle |^2. \tag{2.29}$$

The sum over the unoccupied orbitals and k points of the projection constitutes the number of excited electrons [2]:

$$N_{\mathrm{exc}}(t) = \sum_{j\boldsymbol{k}}^{\mathrm{unocc}} w_{\boldsymbol{k}} m^{\mathrm{e}}_{j\boldsymbol{k}}(t). \tag{2.30}$$

3 Implementation

This section is dedicated to present the implementation of PBE0 and HSE within the RT-TTDFT method in `exciting`. Firstly, the `exciting` code is introduced. In this section, a special focus is put on the basis. Secondly, the implementation of the non-local potential and the non-local current are presented. The implementation of the non-local potential is based on an existing implementation for the GS. In this work, a version with time-dependent KS eigenvectors was implemented and inserted into RT-TDDFT. For the implementation of the non-local current, a discussion about its magnitude and an internal test are presented.

3.1 The `exciting` code

`exciting` is an all-electron full-potential package, providing a wide range of applications from DFT to excited-state calculations [1]. The code employs linearized augmented plane waves (LAPW) plus local orbitals (LO) as basis, which is capable of reaching ultimate precision for solving the KS equations [27].

3.1.1 The LAPW + LO basis functions

Electronic-structure codes aim to represent the KS wave functions $\{\psi_{n\boldsymbol{k}}(\boldsymbol{r}))\}$ in a way that is both accurate and computationally efficient. One common choice is to employ an expansion in terms of basis functions [1]:

$$\psi_{n\boldsymbol{k}}(\boldsymbol{r}) = \sum_{\boldsymbol{G}} C^{\boldsymbol{k}}_{n\boldsymbol{G}} \phi_{\boldsymbol{G}+\boldsymbol{k}}(\boldsymbol{r}), \tag{3.1}$$

where $\boldsymbol{G}$ the G-vector, $C^{\boldsymbol{k}}_{n\boldsymbol{G}}$ denotes the expansion coefficient, and $\phi_{\boldsymbol{G}+\boldsymbol{k}}(\boldsymbol{r})$ the basis functions. These basis functions can be truncated to an incomplete subset that still encompasses the characteristic behavior of the wave function. The idea is to make a trade-off between computational cost and accuracy. For the question of which basis functions to choose, the mathematic properties of the basis functions and behavior of the electrons have to be considered. In the region close to the nuclei, the electrons are highly localized. The wave functions can be considered as rapidly varying, with negligible overlap to wave functions of other atoms. Wave functions in the interstitial (I) regions between atoms exhibit smooth behavior with strong overlap. In regions where the atomic potential is predominantly screened by the core electrons, a plane-wave basis can give a suitable representation of the valence wave functions:

$$P_{\boldsymbol{G}+\boldsymbol{k}}(\boldsymbol{r}) = \frac{1}{\sqrt{\Omega}} \exp\big(\mathrm{i}(\boldsymbol{G}+\boldsymbol{k}) \cdot \boldsymbol{r}\big). \tag{3.2}$$

Plane waves exhibit mathematically favorable aspects. A product of two plane waves is again a plane wave. Furthermore, the fast Fourier transform can be utilized to convert between reciprocal and real space with optimal scaling with respect to problem size [28, 27]. However, in regions near the core, the number of required plane waves grows exceedingly large. Other codes mitigate the problem by replacing the divergent $\frac{1}{\boldsymbol{r}}$ potential with a non-divergent pseudo-potential. Wave functions calculated with the pseudo-potential method are expected to give accurate results for quantities governed by the behavior of electrons outside the core region. However, this approach is not well suited for materials with localized *d*- or *f* orbitals or materials for which the potential is not only screened by the innermost core electrons [28, 27].

Another strategy is to partition the unit cell into muffin-tin (MT) spheres centered at the atomic positions and the remaining I space. The radii of the spheres do not overlap. The augmented plane wave (APW) basis functions $\gamma_{\alpha l m}^{\boldsymbol{G}+\boldsymbol{k}}(\boldsymbol{r})$ inside the MT sphere consist of an expansion in spherical harmonics $Y_{lm}(\hat{\boldsymbol{r}}_\alpha)$ and radial functions $u_{l\alpha}(r_\alpha)$:

$$\gamma_{\alpha l m}^{\boldsymbol{G}+\boldsymbol{k}}(\boldsymbol{r}) = \sum_{lm} A_{lm\alpha}^{\boldsymbol{G}+\boldsymbol{k}} u_{l\alpha}(r_\alpha) Y_{lm}(\hat{\boldsymbol{r}}_\alpha), \tag{3.3}$$

where α denotes an atom index, $\boldsymbol{r}_\alpha$ the vector from the center of α to $\boldsymbol{r}$ ($\boldsymbol{r}_\alpha = \boldsymbol{r} - \boldsymbol{R}_\alpha$), and $A_{lm\alpha}^{\boldsymbol{G}+\boldsymbol{k}}$ the expansion coefficients, which conserve the continuity of the basis functions at the sphere boundary. Inside the MT spheres, the radial functions are obtained via the radial Schrödinger equation:

$$\Big[-\frac{1}{2}\frac{\mathrm{d}^2}{\mathrm{d}r^2} + \frac{l(l+1)}{2r^2} + v_0(r_\alpha) - \epsilon_{n\boldsymbol{k}}\Big]\big(r_\alpha u_{l\alpha}(r_\alpha)\big) = 0, \tag{3.4}$$

where $\epsilon_{n\boldsymbol{k}}$ are the KS energies. Close to the nuclei, it is seen a reasonable approximation to take the spherical average v_0 of the KS potential v_{KS}. One computational challenge of this approach is that the solutions of Eq. 3.4 are itself energy dependent. This potentially complex relation can be approximated by including the first energy derivative of the radial term. Both radial functions are then evaluated at a fixed linearization energy $\epsilon_{l\alpha}$ [27].

With that, the LAPW basis functions inside the MT sphere read:

$$\gamma_{\alpha lm}^{\boldsymbol{G}+\boldsymbol{k}}(\boldsymbol{r}) = \sum_{lm} \Big(A_{lm\alpha}^{\boldsymbol{G}+\boldsymbol{k}} u_{l\alpha}(r_\alpha; \epsilon_{l\alpha}) + B_{lm\alpha}^{\boldsymbol{G}+\boldsymbol{k}} \frac{\partial u_{l\alpha}(r_\alpha, \epsilon)}{\partial \epsilon}\Big|_{\epsilon=\epsilon_{l\alpha}} \Big) Y_{lm}(\hat{\boldsymbol{r}}_\alpha). \tag{3.5}$$

where, in addition to $A_{lm\alpha}^{\boldsymbol{G}+\boldsymbol{k}}$, $B_{lm\alpha}^{\boldsymbol{G}+\boldsymbol{k}}$ is determined as to ensure the continuity of the first derivation at the MT boundary. The full LAPW basis functions across the unit cell are given by:

$$\phi_{\boldsymbol{G}+\boldsymbol{k}}(\boldsymbol{r}) = \begin{cases} \gamma_{\alpha lm}^{\boldsymbol{G}+\boldsymbol{k}}(\boldsymbol{r}) & \boldsymbol{r} \in MT_\alpha \\ P_{\boldsymbol{G}+\boldsymbol{k}}(\boldsymbol{r}) & \boldsymbol{r} \in I. \end{cases} \tag{3.6}$$

The error of this linear approximation was found to be of the order of $(\epsilon - \epsilon_{l\alpha})^4$ for the band energies [1]. The basis can be supplemented with additional functions in the form of LOs, which are evaluated at a different KS energy $\epsilon'_{l\alpha}$:

$$\phi_{\alpha lm}^{\mathrm{LO}}(\boldsymbol{r}) = \begin{cases} \sum_{lm} \Big[A_{lm\alpha}^{\mathrm{LO}} u_{l\alpha}(r_\alpha; \epsilon_{l\alpha}) + B_{lm\alpha}^{\mathrm{LO}} \dot{u}_{l\alpha}(r_\alpha; \epsilon_{l\alpha}) + C_{lm\alpha}^{\mathrm{LO}} u_{l\alpha}(r_\alpha; \epsilon'_{l\alpha})) \Big] Y_{lm}(\hat{\boldsymbol{r}}_\alpha) & \boldsymbol{r} \in MT_\alpha \\ 0 & \boldsymbol{r} \in I. \end{cases} \tag{3.7}$$

These functions are zero in the I region and are well suited for the description of semicore states. Finally, the LAPW+LO basis is then formed by supplementing the functions of Eq. 3.6 with the LOs of Eq. 3.7. In `exciting`, `rgkmax` determines the number of APW's in the basis [1]. It is formed by the product of two quantities: The smallest muffin tin radius and the maximum length of the $\boldsymbol{G} + \boldsymbol{k}$ vector [1]. Together with the number of LO's, `rgkmax` controls the completeness of the basis.

3.1.2 Mixed product basis

For expressions that contain a product of two KS wave functions, which is the case for hybrid functionals, a product basis can be employed. The LAPW+LO basis is continuous, but has distinct parts for different spatial regions. The product basis can be constructed in such a way that it is defined in one region and zero in the other. The mixed product basis (MPB) $\{\chi_i^{\boldsymbol{q}}\}$ is given by:

$$\psi_{n\boldsymbol{k}}(\boldsymbol{r}, t)\psi_{m\boldsymbol{k}-\boldsymbol{q}}^*(\boldsymbol{r}, t) = \sum_i M_{nm}^i(\boldsymbol{k}, \boldsymbol{q}, t)\chi_i^{\boldsymbol{q}}(\boldsymbol{r}). \tag{3.8}$$

It is constructed from plane waves in the I region and from spherical harmonics in the MT region. The corresponding expansion coefficients are given by:

$$M_{nm}^i(\boldsymbol{k}, \boldsymbol{q}, t) = \int_\Omega \big(\chi_i^{\boldsymbol{q}}(\boldsymbol{r})\psi_{m\boldsymbol{k}-\boldsymbol{q}}(\boldsymbol{r}, t)\big)^* \psi_{n\boldsymbol{k}}(\boldsymbol{r}, t) d\boldsymbol{r}. \tag{3.9}$$

3.2 Implementation of RT-TDDFT with hybrids

The implementation of RT-TDDFT with hybrids requires the incorporation of the non-local potential. Firstly, the non-local potential needs to be included in the Hamiltonian and propagated in time. Secondly, there occurs an additional term for the current density, the non-local current density. This section is dedicated to derive the formulas for the computation of the matrix elements of the non-local potential and non-local current density.

3.2.1 Matrix form of the non-local potential

The construction of the non-local potential was already implemented for the GS cycle of `exciting`. For RT-TDDFT, this implementation was modified to built the non-local potential from the time-dependent wave functions. The non-local potential of Eq. 2.14 can be formulated in reciprocal space as:

$$v_{\mathrm{NL}}^{nm}(\boldsymbol{k},t) = -\sum_{n''}^{\mathrm{occ.}}\sum_{\boldsymbol{q}}^{\mathrm{BZ}}\int\int \frac{\psi_{n\boldsymbol{k}}^{*}(\boldsymbol{r},t)\psi_{n''\boldsymbol{q}}(\boldsymbol{r},t)\psi_{n''\boldsymbol{q}}^{*}(\boldsymbol{r}',t)\psi_{m\boldsymbol{k}}^{*}(\boldsymbol{r}',t)}{|\boldsymbol{r}-\boldsymbol{r}'|}d\boldsymbol{r}d\boldsymbol{r}'. \tag{3.10}$$

The matrix elements of this six dimensional integral are computationally expensive to evaluate. One way to reduce the cost is by choosing a cutoff, N_{empty}, for the state indices n and m. Although all states are involved in forming the non-local potential, the energetically higher states are expected to have consecutively less impact. Due to their locality, the core states are expected to give us computational cheap expressions for the non-local potential. For the explicitly k-dependent valence states, the cost of this operation can be reduced by employing the MPB. It gives a more efficient description by confining the wave function products to either the MT or the I region. This transforms Eq. 3.10 into a vector-matrix-vector product, where all components are given in the MPB representation:

$$v_{\mathrm{NL}}^{nm}(\boldsymbol{k},t) = -\sum_{n''}^{occ}\sum_{ij\boldsymbol{q}}\left(M_{nn''}^{i}(\boldsymbol{k},\boldsymbol{q},t)\right)^{*}v_{ij}(\boldsymbol{q})M_{mn''}^{j}(\boldsymbol{k},\boldsymbol{q},t). \tag{3.11}$$

The decomposition of the Coulomb matrix $v_{ij}(\boldsymbol{q})$ can be written as:

$$v_{ij}(\boldsymbol{q}) = \int_{V}\left(\chi_{i}^{\boldsymbol{q}}(\boldsymbol{r})\right)^{*}\frac{1}{|\boldsymbol{r}-\boldsymbol{r}'|}\chi_{j}^{\boldsymbol{q}}(\boldsymbol{r}')d\boldsymbol{r}d\boldsymbol{r}'. \tag{3.12}$$

This expression is wave-function independent and can be evaluated before the expansion coefficients $M_{nn''}^{i}(\boldsymbol{k},\boldsymbol{q},t)$ are constructed. It can be rewritten with the help of the Fourier transform of the Coulomb interaction:

$$\frac{1}{|\boldsymbol{r}-\boldsymbol{r}'|}=\frac{1}{V}\sum_{\boldsymbol{qG}}e^{\mathrm{i}(\boldsymbol{q}+\boldsymbol{G})\boldsymbol{r}}\frac{4\pi}{|\boldsymbol{q}+\boldsymbol{G}|^2}e^{-\mathrm{i}(\boldsymbol{q}+\boldsymbol{G})\boldsymbol{r}'}, \tag{3.13}$$

which is diagonal in plane wave representation. This simple plane wave representation can be extended into the mixed basis via the overlap $W^i_{\mathbf{G}}(\boldsymbol{q})$ between the LAPW+LO basis and the plane waves:

$$v_{ij}(\boldsymbol{q})=\sum_{\mathbf{G}}W^i_{\mathbf{G}}(\boldsymbol{q})\frac{4\pi}{|\boldsymbol{q}+\mathbf{G}|^2}\left(W^j_{\mathbf{G}}(\boldsymbol{q})\right)^*, \tag{3.14}$$

where the overlap is given by:

$$W^i_{\boldsymbol{G}}(\boldsymbol{q})=\frac{1}{\sqrt{\Omega}}\int_\Omega\left(\chi^{\boldsymbol{q}}_i(\boldsymbol{r})\right)^*\exp\left(\mathrm{i}(\boldsymbol{q}+\boldsymbol{G})\boldsymbol{r}\right)d\boldsymbol{r}. \tag{3.15}$$

This overlap is straightforward in the I region, where plane waves are used in the mixed basis. There is an alternative way to rewrite Eq. 3.11 to give analytical expressions for the *MT-MT*, *I-I*, *MT-I*, and *I-MT* parts of the mixed-basis product [29, 28]. Both modes were already implemented in `exciting`. For computational purposes, expression 3.11 is often written in a more compact form with the help of the matrix elements $\tilde{M}^i_{mn''}(\boldsymbol{k},\boldsymbol{q},t)$. These contract the square root of the Coulomb expression and the expansion coefficients as:

$$\tilde{M}^i_{mn''}(\boldsymbol{k},\boldsymbol{q},t)=\sum_j\left(v_{ij}(\boldsymbol{q})\right)^{\frac{1}{2}}M^j_{mn''}(\boldsymbol{k},\boldsymbol{q},t).$$

For this purpose, the Coulomb matrix in the LAPW basis (Eq. 3.14) is diagonalized, all eigenvalues below zero are discarded, and the matrix is reconstructed with the square root of the eigenvalues and the eigenvectors. Since the final expression is constructed symmetrically, it is only necessary to make the product with the eigenvalues on one side of the reconstructed matrix. With that, the compact expression takes the form:

$$v^{nm}_{\mathrm{NL}}(\boldsymbol{k},t)=-\sum_{n''}^{occ}\sum_{ij\boldsymbol{q}}\left(\tilde{M}^i_{nn''}(\boldsymbol{k},\boldsymbol{q},t)\right)^*\tilde{M}^j_{mn''}(\boldsymbol{k},\boldsymbol{q},t). \tag{3.16}$$

The non-local potential is then included in the Hamiltonian in LAPW+LO basis:

$$v^{\boldsymbol{GG}'}_{\mathrm{NL}}(\boldsymbol{k},t)=\sum_{n,n'}^{occ+unocc}\big[\sum_{\boldsymbol{G}''}S^*_{\boldsymbol{GG}''}(\boldsymbol{k})c_{\boldsymbol{G}''}(n,\boldsymbol{k},t)\big]v^{nn'}_{\mathrm{NL}}(\boldsymbol{k},t)\big[\sum_{\boldsymbol{G}''}S_{\boldsymbol{G}'\boldsymbol{G}''}(\boldsymbol{k})c^*_{\boldsymbol{G}''}(n',\boldsymbol{k},t)\big], \tag{3.17}$$

where S denotes the overlap matrix and c the coefficients of the KS state. The wave functions are then evolved for each time step according to Eq. 2.23 By default, a RT-TDDFT calculation with `exciting` performs a one-step GS calculation with the given excited-state convergence parameters, which takes the saved electronic density and potentials from the GS calculation. This one shot calculation then provides the density and the KS wave functions of the following RT-TDDFT calculation. This scheme can be used to perform a highly converged GS- and less computationally expensive RT-TDDFT run. However, for a RT-TDDFT calculation with hybrids, the same convergence parameters of the GS should be used for the excited state. For that reason, the convergence parameters of the GS are automatically applied to a RT-TDDFT calculation with hybrids. The one shot calculation is skipped and densities, wave functions and potentials are read from the GS.

3.2.2 Matrix form of the non-local current

The non-local current stems from the commutator between the non-local potential and spatial operator, as is derived from Eq. 2.25. The expectation value over the many-body wave function can be formulated in terms of KS wave functions:

$$\boldsymbol{J}_{\mathrm{NL}}(t) = \alpha \frac{\mathrm{i}}{\Omega} \sum_{n\boldsymbol{k}}^{\mathrm{occ}} w_{\boldsymbol{k}} f_{n\boldsymbol{k}} \left\langle \psi_{n\boldsymbol{k}}(t) \right| [\boldsymbol{r}, \hat{v}_{\mathrm{X}}^{\mathrm{NL}}] \left| \psi_{n\boldsymbol{k}}(t) \right\rangle , \tag{3.18}$$

Where Ω is the unit cell volume, $w_{\boldsymbol{k}}$ the weight of the $\boldsymbol{k}$ points, and $f_{n\boldsymbol{k}}$ the occupation of the KS state. The sum in this expression goes only over the valence states. The non-local potential acts in the expectation value of the state $\psi_{n\boldsymbol{k}}$ according to Eq. 3.10 in which the sum goes over valence and core states.

$$\int \big(\psi_{n\boldsymbol{k}}(\boldsymbol{r},t)\big)^{*} \hat{V}_{\mathrm{NL}} \psi_{n\boldsymbol{k}}(\boldsymbol{r},t) d\boldsymbol{r} = -\sum_{m}^{\mathrm{occ.}} \sum_{\boldsymbol{q}}^{\mathrm{BZ}} \int \int \frac{\big(\psi_{n\boldsymbol{k}}(\boldsymbol{r},t)\big)^{*} \psi_{m\boldsymbol{q}}(\boldsymbol{r},t) \big(\psi_{m\boldsymbol{q}}(\boldsymbol{r}',t)\big)^{*} \psi_{n\boldsymbol{k}}(\boldsymbol{r}',t)}{|\boldsymbol{r}-\boldsymbol{r}'|} d\boldsymbol{r}' d\boldsymbol{r} \tag{3.19}$$

With that, the non-local current can be written as:

$$\begin{aligned} \boldsymbol{J}_{\mathrm{NL}}(t) = -\alpha \frac{\mathrm{i}}{\Omega} \sum_{\boldsymbol{k}\boldsymbol{k}'} \sum_{nm} w_{\boldsymbol{k}} f_{n\boldsymbol{k}} w_{\boldsymbol{k}'} f_{m\boldsymbol{k}'} \int_{\Omega} \int_{V} \psi_{m\boldsymbol{k}'}(\boldsymbol{r},t) \big(\psi_{n\boldsymbol{k}}(\boldsymbol{r},t)\big)^{*} \frac{(\boldsymbol{r}-\boldsymbol{r'})}{|\boldsymbol{r}-\boldsymbol{r}'|} & \\ * \big(\psi_{m\boldsymbol{k}'}(\boldsymbol{r'},t)\big)^{*} \psi_{n\boldsymbol{k}}(\boldsymbol{r'},t) d\boldsymbol{r} d\boldsymbol{r'}, & \end{aligned} \tag{3.20}$$

where the sum over n goes over valence states and the sum over m over core and valence states. This expression can, analogous to the non-local potential, be decomposed into a vector-matrix-vector product. In the MPB representation (Eq. 3.8), the product of two

KS wave functions can be written as:

$$\boldsymbol{J}_{\mathrm{NL}}(t) = -\alpha\frac{\mathrm{i}}{\Omega}\sum_{ijnm\boldsymbol{kq}} w_{\boldsymbol{k}} f_{n\boldsymbol{k}} w_{\boldsymbol{k}-\boldsymbol{q}} f_{m\boldsymbol{k}-\boldsymbol{q}} \big(M^{j}_{nm}(\boldsymbol{k},\boldsymbol{q},t)\big)^{*}$$
$$* \int_{\Omega}\int_{V} \big(\chi^{\boldsymbol{q}}_{j}(\boldsymbol{r})\big)^{*} \frac{(\boldsymbol{r}-\boldsymbol{r'})}{|\boldsymbol{r}-\boldsymbol{r'}|} \chi^{\boldsymbol{q}}_{i}(\boldsymbol{r'}) d\boldsymbol{r} d\boldsymbol{r'} * M^{i}_{nm}(\boldsymbol{k},\boldsymbol{q},t), \quad (3.21)$$

where the expansion coefficients $M^{j}_{nm}(\boldsymbol{k},\boldsymbol{q},t)$ exhibit an explicit dependence on the $\boldsymbol{k}$- and $\boldsymbol{q}$ points for the valence states. The last term contains the MPB and the remaining spatial dependence. It can be rewritten with the help of the Fourier transform, which is given by:

$$\frac{(\boldsymbol{r}-\boldsymbol{r'})}{|\boldsymbol{r}-\boldsymbol{r'}|} = \sum_{\boldsymbol{qG}} e^{\mathrm{i}(\boldsymbol{q}+\boldsymbol{G})\boldsymbol{r}} \boldsymbol{F}^{\boldsymbol{q}}_{\boldsymbol{G}} e^{-\mathrm{i}(\boldsymbol{q}+\boldsymbol{G})\boldsymbol{r}'}, \quad (3.22)$$

where for PBE0, $\boldsymbol{F}^{\boldsymbol{q}}_{\boldsymbol{G}}$ takes the form:

$$\boldsymbol{F}^{\boldsymbol{q}}_{\boldsymbol{G}} = \begin{cases} -\frac{8\pi\mathrm{i}(\boldsymbol{q}+\boldsymbol{G})}{|\boldsymbol{q}+\boldsymbol{G}|^{4}}, & \boldsymbol{q}+\boldsymbol{G}\neq 0 \\ \boldsymbol{0}, & \boldsymbol{q}+\boldsymbol{G}=0. \end{cases} \quad (3.23)$$

The derivation for HSE06 is more involved than for PBE0, but follows the same path. A full derivation of the Fourier transform is given in appendix 6.1. The expression takes the form:

$$\boldsymbol{F}^{\boldsymbol{q}}_{\boldsymbol{G}} = \begin{cases} \frac{8\pi\mathrm{i}(\boldsymbol{q}+\boldsymbol{G})}{|\boldsymbol{q}+\boldsymbol{G}|^{4}}\left[-1+\exp\left(\frac{-(\boldsymbol{q}+\boldsymbol{G})^{2}}{4\omega^{2}}\right)\left(1+\frac{(\boldsymbol{q}+\boldsymbol{G})^{2}}{4\omega^{2}}\right)\right], & \boldsymbol{q}+\boldsymbol{G}\neq 0 \\ \boldsymbol{0}, & \boldsymbol{q}+\boldsymbol{G}=0, \end{cases}$$

It leads to Eq. 3.23 for $\omega \to 0$ and to 0 for $\omega \to \infty$. The expression can be rewritten in the same manner as Eq. 3.14, where the overlap $W^{i}_{\boldsymbol{G}}$ (Eq. 3.15) is used: A contraction of this term, similar to Eq. 3.16, is not admissible since the Fourier transform $\boldsymbol{F}^{\boldsymbol{q}}_{\boldsymbol{G}}$ may contain negative diagonal elements. Overall, the implemented equation can be written as:

$$\boldsymbol{J}_{\mathrm{NL}}(t) = -\alpha\frac{\mathrm{i}}{\Omega}\sum_{ijnm\boldsymbol{kq}} w_{\boldsymbol{k}} f_{n\boldsymbol{k}} w_{\boldsymbol{k}-\boldsymbol{q}} f_{m\boldsymbol{k}-\boldsymbol{q}} \big(M^{j}_{nm}(\boldsymbol{k},\boldsymbol{q},t)\big)^{*} \boldsymbol{F}^{\boldsymbol{q}}_{\boldsymbol{G}} M^{i}_{nm}(\boldsymbol{k},\boldsymbol{q},t). \quad (3.24)$$

To investigate the non-local current, the symmetry of J_{NL} with regard to the states and $\boldsymbol{k}$ points can be analyzed. To this end, a partial sum of Eq. 3.24 can be built:

$$\begin{aligned} \boldsymbol{J}_{\mathrm{NL}}(t) &= -\alpha\frac{\mathrm{i}}{\Omega}\sum_{ijnm\boldsymbol{kq}} w_{\boldsymbol{k}} f_{n\boldsymbol{k}} w_{\boldsymbol{k}-\boldsymbol{q}} f_{m\boldsymbol{k}-\boldsymbol{q}} \big(M^{j}_{nm}(\boldsymbol{k},\boldsymbol{q},t)\big)^{*} M^{i}_{nm}(\boldsymbol{k},\boldsymbol{q},t) \\ &\quad * \int_{\Omega}\int_{V} \boldsymbol{F}(\boldsymbol{r},\boldsymbol{r'}) \big(\chi^{\boldsymbol{q}}_{j}(\boldsymbol{r})\big)^{*} \chi^{\boldsymbol{k}}_{i}(\boldsymbol{r'}) d\boldsymbol{r} d\boldsymbol{r'} \\ &= -\alpha\frac{\mathrm{i}}{\Omega}\sum_{ijnm\boldsymbol{kq}} w_{\boldsymbol{k}} f_{n\boldsymbol{k}} w_{\boldsymbol{k}-\boldsymbol{q}} f_{m\boldsymbol{k}-\boldsymbol{q}} \boldsymbol{j}^{nm}_{\mathrm{part}}(t,i,j,\boldsymbol{k},\boldsymbol{q}). \end{aligned}$$

It can be observed, that $\boldsymbol{F}(\boldsymbol{r},\boldsymbol{r'}) = -\boldsymbol{F}(\boldsymbol{r'},\boldsymbol{r})$. When the indices are switched ($\boldsymbol{k} \leftrightarrow \boldsymbol{q}$, $n \leftrightarrow m$), the symmetry of $\boldsymbol{F}$ changes the prefactor of $\boldsymbol{j}^{nm}_{\text{part}}(t,i,j,\boldsymbol{k},\boldsymbol{q})$ so that:

$$\begin{aligned}
&\boldsymbol{j}^{nm}_{\text{part}}(t,i,j,\boldsymbol{k},\boldsymbol{q}) = \psi_{m\boldsymbol{k'}}(\boldsymbol{r},t)\big(\psi_{n\boldsymbol{k}}(\boldsymbol{r},t)\big)^{*}\boldsymbol{F}(\boldsymbol{r},\boldsymbol{r'})\big(\psi_{m\boldsymbol{k'}}(\boldsymbol{r'},t)\big)^{*}\psi_{n\boldsymbol{k}}(\boldsymbol{r'},t)d\boldsymbol{r}d\boldsymbol{r'},\\
&\boldsymbol{j}^{mn}_{\text{part}}(t,i,j,\boldsymbol{q},\boldsymbol{k}) = \psi_{m\boldsymbol{k'}}(\boldsymbol{r'},t)\big(\psi_{n\boldsymbol{k}}(\boldsymbol{r'},t)\big)^{*}\boldsymbol{F}(\boldsymbol{r},\boldsymbol{r'})\big(\psi_{m\boldsymbol{k'}}(\boldsymbol{r},t)\big)^{*}\psi_{n\boldsymbol{k}}(\boldsymbol{r},t)d\boldsymbol{r'}d\boldsymbol{r},\\
&\boldsymbol{j}^{nm}_{\text{part}}(t,i,j,\boldsymbol{k},\boldsymbol{q}) = -\boldsymbol{j}^{mn}_{\text{part}}(t,i,j,\boldsymbol{q},\boldsymbol{k}).
\end{aligned}$$

With that, one would expect the non-local current to cancel out in the sum over the states. However, the non-local current is small but nonzero for diamond, given in Fig. 12. The origin of this is in the construction of the non-local current. There are two sums over the states, one from the definition of the current and one from the non-local potential. The sum originating from the definition of the current does not include the core states. With this, the two sums can not cancel each other out.

Since we can not conduct a 1 to 1 comparison with other codes, another method of testing was devised. In order to test if the implementation of $\boldsymbol{J}_{\text{NL}}(t)$, a consistency check with the implementation of $v^{nm}_{\text{NL}}(\boldsymbol{k},t)$ can be performed. Equation 3.11 and equation 3.21 share a similar structure. When the Fourier transform of the commutator $\boldsymbol{F}^{\boldsymbol{q}}_{\boldsymbol{G}}$ is replaced with the Fourier transform of the Coulomb potential (Eq. 3.13) in $\boldsymbol{J}_{\text{NL}}(t)$, the summands of $\boldsymbol{J}_{\text{NL}}(t)$ and v^{nn}_{NL} have the same value:

$$\begin{aligned}
v^{nm}_{\text{NL}}(\boldsymbol{k},t) &= -\sum_{m}^{occ}\sum_{ij\boldsymbol{q}}\big(M^{i}_{nm}(\boldsymbol{k},\boldsymbol{q},t)\big)^{*}v_{ij}(\boldsymbol{q})M^{j}_{m'm}(\boldsymbol{k},\boldsymbol{q},t)\\
&= -\sum_{m}^{occ}\sum_{ij\boldsymbol{q}}V^{nm'm}_{\text{part}}(t,i,j,\boldsymbol{k},\boldsymbol{q}).
\end{aligned}$$

For $m' = n$:

$$v^{nn}_{\text{NL}}(\boldsymbol{k},t) = -\sum_{m}^{occ}\sum_{ij\boldsymbol{q}}V^{nm}_{\text{part}}(t,i,j,\boldsymbol{k},\boldsymbol{q}).$$

With that, the elements of the partial sums should be equal, given that $\boldsymbol{F}^{\boldsymbol{q}}_{\boldsymbol{G}} = v_{ij}(\boldsymbol{q})$ in $\boldsymbol{J}_{\text{NL}}(t)$:

$$V^{nm}_{\text{part}}(t,i,j,\boldsymbol{k},\boldsymbol{q}) = (\boldsymbol{j}^{nm}_{\text{part}}(t,i,j,\boldsymbol{k},\boldsymbol{q}))_{x,y,z} \tag{3.25}$$

The partial sum for $\boldsymbol{J}_{\text{NL}}(t)$ is built with the Fourier transform of the Coulomb potential and compared when the option `testJNL` is set as true in the `realTimeTDDFT` element of the input file. The largest difference of all indices is written out for each time step. When the difference between the elements of the partial sums of Eq. 3.25 exceeds 10^{-10}, the program stops.

4 Results

This section is dedicated to present the results of the implementation. In section 4.1, we consider diamond and in section 4.2, boron nitride. To validate the implementation, we focus on the induced current density and the number of excited electrons. The first includes the non-local current, and the second gives information about the time evolution of the system. For both materials, first convergence tests for the GS are performed with PBE and PBE0. Afterwards, the impact of the convergence parameters on J_{ind} and N_{exc} is investigated. Then, the impact of the functionals on J_{ind} and N_{exc} is investigated. HSE calculations with the convergence parameters of PBE0 are presented for diamond. For HSE, ω is varied to investigate the transition to PBE. Then, the results are compared with the octopus code as a means to validate the implementation. Furthermore, the results of the internal test for the non-local current are shown.

4.1 Diamond

Diamond consists of carbon atoms, bound with 4 neighbors via hybridized sp^3 orbitals, and has an indirect gap of $E_g = 5.47$ eV [30]. As an insulator, diamond is well suited to test the implementation of the PBE0 functional.

4.1.1 Computational details

Diamond's structure was chosen in its most common face cubic centered configuration with a lattice constant of 3.43 Å. The number of k points was chosen as 3x3x3 for all calculations. Although this number of k points does not provide a basis for in depth characterization of the physical attributes of diamond, it should be sufficient to validate the implementation. For the GS, convergence tests were conducted for `rgkmax` with PBE and PBE0 and for the number of empty states (N_{empty}) with PBE0. For the other basis paramters, when not specifically stated otherwise, one LO with l=0 and one LO with l=1 are used for the following diamond calculations. N_{empty} specifies the number of unoccupied eigenstates. This parameter has an impact on the energy gaps of hybrid calculations via the non-local potential (Eq. 3.17).

The band gaps between CB and VB for `rgkmax` and N_{empty} are listed in Tab. 1 and

Tab. 2 respectively. Generally, the smallest energy gap was found at the transition from Γ to $(0.\overline{6}, 0.\overline{6}, 0)$. For `rgkmax` $= 6$, the GS energies are converged up to 10 meV. The convergence with respect to N_{empty} seems swift and $N_{\text{empty}} = 20$ can already be seen as converged. Furthermore, calculations for different ω were conducted. For these, `rgkmax` $= 6$ and $N_{\text{empty}} = 20$ was chosen. Band gaps for different ω are listed in Tab. 3. As expected, the band gaps are similar to PBE at large values for ω and approach the PBE0 value for smaller values.

Table 1: Band gaps (in eV) of diamond for different values of `rgkmax` obtained with the PBE and PBE0 functional. Listed are the eigenvalue differences from Γ to Γ and from Γ to $(0.\overline{6}, 0.\overline{6}, 0)$.

	$E_{\Gamma-\Gamma}$		$E_{\Gamma-(0.\overline{6},\ 0.\overline{6},\ 0)}$	
`rgkmax`	PBE	PBE0	PBE	PBE0
4	5.39	7.81	3.81	5.99
5	5.62	8.02	4.17	6.36
6	5.58	7.99	4.12	6.32
7	5.57	7.98	4.12	6.32

Table 2: Band gaps (in eV) for different values of N_{empty}, calculated with the PBE0 functional. For, `rgkmax` the value of 5 was chosen.

N_{empty}	$E_{\Gamma-\Gamma}$	$E_{\Gamma-(0.\overline{6},\ 0.\overline{6},\ 0)}$
10	7.81	6.39
20	8.02	6.36
30	7.99	6.35
40	7.98	6.35

Table 3: Band gaps (in eV) for different ω, with PBE and PBE0. For these, `rgkmax` $= 5$ and $N_{\text{empty}} = 20$ was chosen.

ω	$E_{\Gamma-\Gamma}$	$E_{\Gamma-(0.\overline{6},\ 0.\overline{6},\ 0)}$
0.11	5.72	7.39
0.15	5.32	6.98
0.2	5.05	6.71
0.25	4.87	6.52
0.3	4.73	6.37
1	4.17	5.62
PBE	4.17	5.62
PBE0	6.36	8.02

As a perturbation, a field along the [100] direction was applied, which takes the form:

$$E(t) = E_0 \cos(\omega t + \phi) f(t). \tag{4.1}$$

The amplitude E_0 was chosen as 10 atomic units (a.u.), the angular frequency ω as 1 a.u., and the phase ϕ as 0. The specified laser pulse is given in Fig. 1 (solid line). The envelope function takes a trapezoidal form, which rises from zero at $t = 0$ to one for a rise time, stays at one for a width and goes back to zero for the same rise time. The rise time was chosen as 1 a.u. and the width as 30 a.u. The envelope function times the amplitude $(f(t) \cdot E_0)$ is given as a dotted line in Fig. 1. For all calculations, the approximate enforced time-reversal symmetry propagator was used.

4.1.2 Convergence behavior of RT-TDDFT with hybrids

For the RT-TDDFT calculation, the analyzed convergence parameters include `rgkmax`, the time step (Δt), and N_{empty}. For these parameters, calculations for N_{exc} and J_{ind} were performed with the PBE and the PBE0 functional. For the other parameters `rgkmax`$= 5$, $\Delta t = 0.05$ and $N_{\text{empty}} = 20$ was used as a default.

To analyze the convergence behavior, we use the root-mean-square error (RMSE),

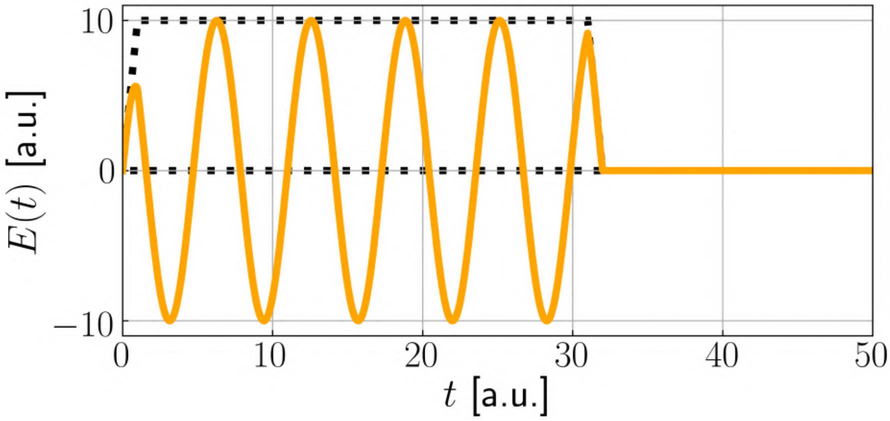

Figure 1: Laser pulse used for diamond. The dotted line shows the trapezoidal envelope function times the amplitude.

$$\text{RMSE} = \sqrt{\frac{\int_{t_{start}}^{t_{end}} \left(Y - Y_{\text{ref}}\right)^2 dt}{T}}, \tag{4.2}$$

where Y refers to either J_{ind} or N_{exc}, Y_{ref} is the corresponding reference value, and T stands for the difference between the start and the end time. The RMSE can be used as a metric which allows us to evaluate the convergence behavior. Y_{ref} is given by the calculation with the best convergence parameter.

In the following, the convergence behavior of J_{ind} or N_{exc} with the PBE0 functional is analyzed. Apart from N_{empty}, the convergence behavior with PBE is very similar to PBE0 and is shown in Appendix 6.2. Firstly, the convergence behavior of J_{ind} and N_{exc} for `rgkmax` was inspected (Fig. 2). With respect to `rgkmax`, for both J_{ind} and N_{exc}, the RMSE decreases quickly. For J_{ind}, the impact of smaller basis size is more pronounced after the laser is turned off. This effect is more pronounced with the PBE functional, which is shown in Fig. 22. For N_{exc}, a smaller basis size corresponds to a lower value of N_{exc}, although the effect is very minor for `rgkmax`≥ 5.

The convergence with respect to Δt was inspected. J_{ind} and N_{exc} are given in Fig. 3. The curves are seemingly identical to the eyesight, which suggests a fast convergence. A time step above 0.3 a.u, which approximately represents the inverse of the largest eigenvalue, leads to divergence and is not shown here.

Lastly, the convergence behavior with respect to the N_{empty} was inspected. J_{ind} and N_{exc} for PBE are given in Fig. 4. Since N_{empty} does not impact the PBE Hamiltonian, it has no effect on J_{ind}. For N_{exc}, the convergence is fast with respect to N_{empty}. For 10 empty states, N_{exc} does not plateau after the laser pulse is turned off, but decreases by 0.0011. Furthermore, the total number of electrons decreases by 0.013 from 0 to 50 time units. This suggests that there are states missing on which to project the GS (Eq. 2.30). The KS wave functions for occupied and unoccupied states do not form a complete set in this case. For PBE0, the convergence behavior is given in Fig. 5. N_{empty} has a more pronounced influence on the PBE0 calculations. Contrary to the PBE Hamiltonian, the PBE0 Hamiltonian is sensitive to N_{exc} throu $v_{\text{NL}}(t)$ (Eq. 3.17). This impacts the band gaps listed in Tab. 2. The differences in the GS and the inclusion of $v_{\text{NL}}(t)$ impact the evolution of the system. For that reason, J_{ind} becomes sensitive to N_{empty}. For N_{exc}=10, the decrease after the laser is turned off becomes more pronounced, with a difference of 0.024. The number of total electrons decreases by 0.035 from 0 to 50 time steps.

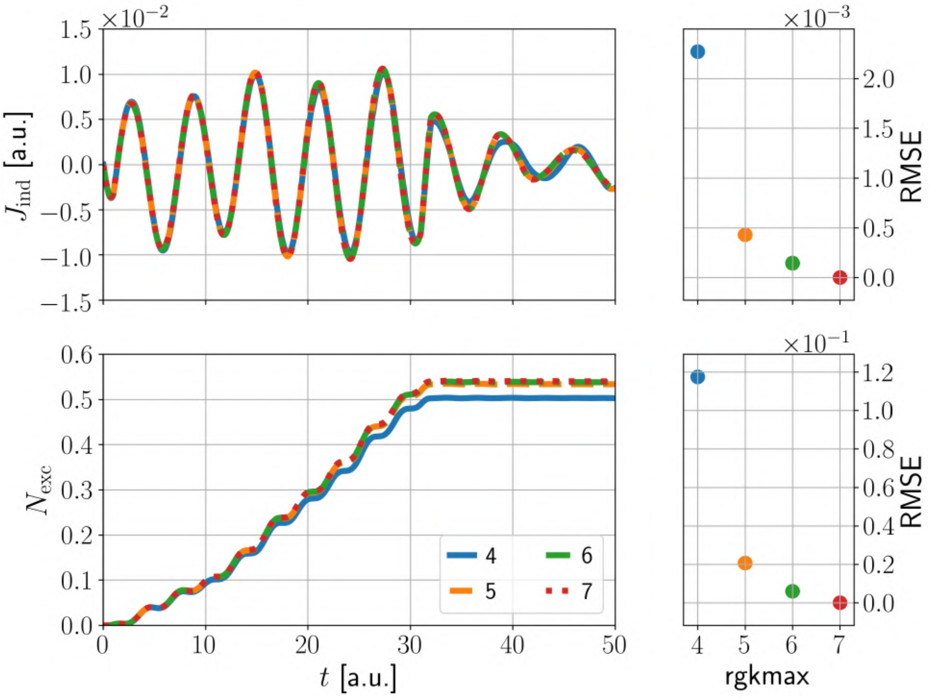

Figure 2: Convergence behavior of J_{ind} and N_{exc} with respect to `rgkmax` for diamond. The used functional was PBE0. `rgkmax`$= 7$ was used as reference.

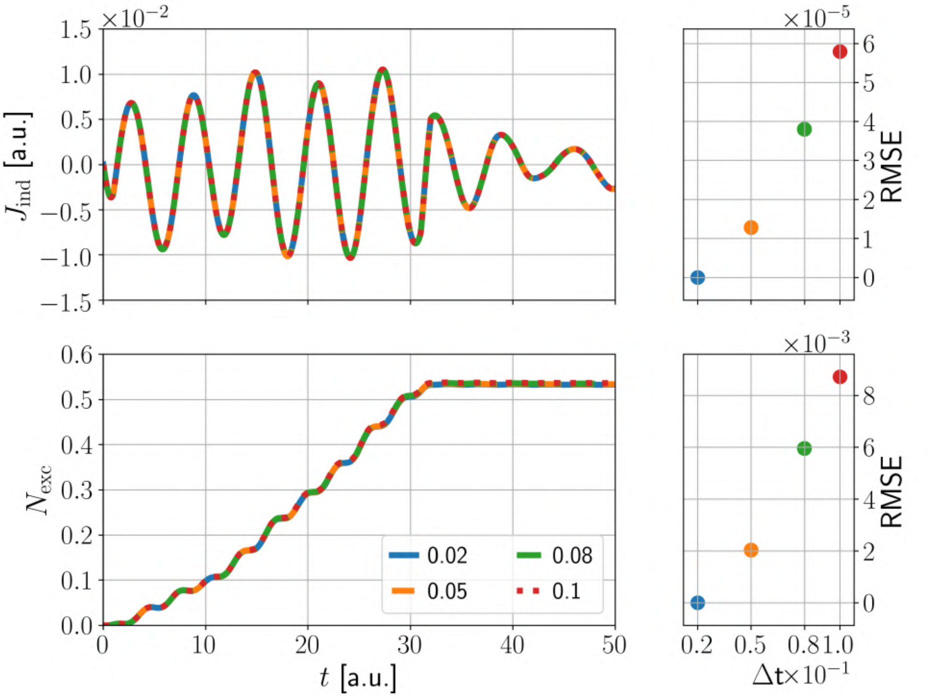

Figure 3: Same as Fig. 2 but with respect to Δt. $\Delta t = 0.02$ was used as reference.

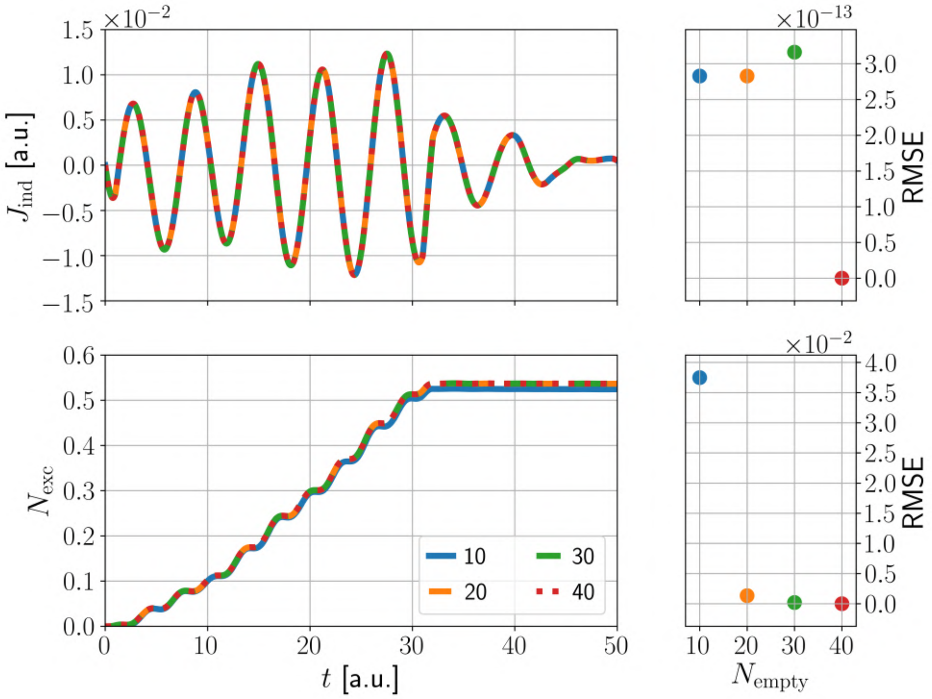

Figure 4: Same as Fig. 2 but with respect to N_{empty} and the used functional is PBE. $N_{\text{empty}} = 40$ was used as reference.

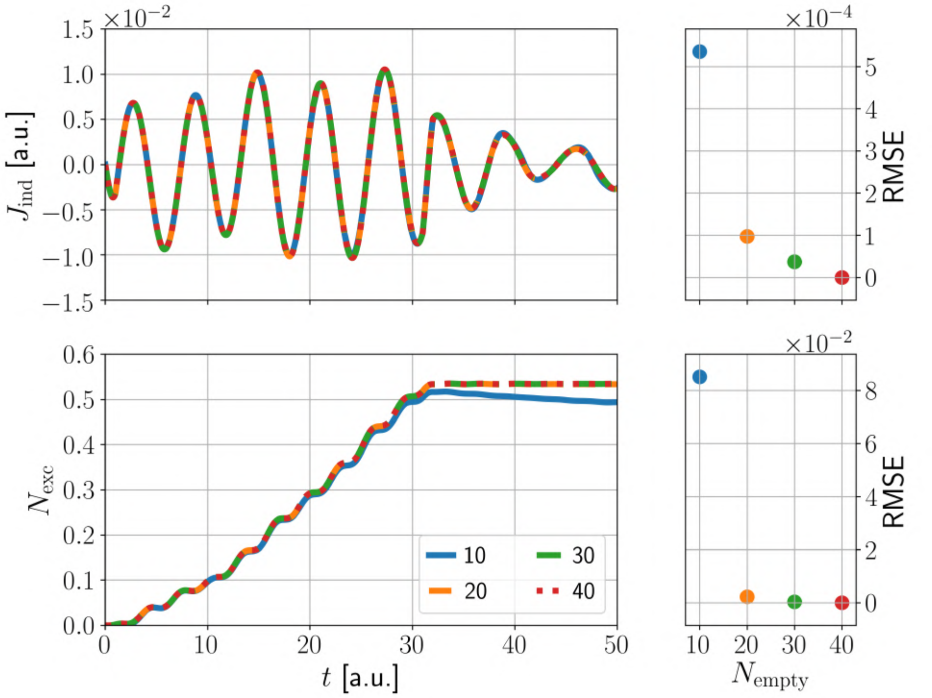

Figure 5: Same as Fig. 2 but with respect to N_{empty}. $N_{\text{empty}} = 40$ was used as reference.

4.1.3 Comparison between PBE and PBE0

After the computational parameters are sufficiently converged, we can turn to analyze the effect of the functionals. J_{ind} and N_{exc} for PBE and PBE0 are given in Fig. 6. N_{exc} seems largely unaffected by the choice of functionals. One explanation for the small impact can be that the amplitude of the laser far exceeds the impact of the two functionals on the band gap. However, it is notable that the difference is largest while the laser is applied. The difference for J_{ind} is largest at the maxima and minima of the laser pulse, the difference growing with the time the system is under the influence of the laser. When the laser is turned off, the two curves converge at first and then grow apart again. Since J_{NL} is of the order of 10^{-5} and J_{dia} is only dependent on the vector potential, the difference is almost exclusively due to J_{para}. At the end of the laser pulse, current response with PBE is larger than with PBE0. This is consistent with the band gaps.

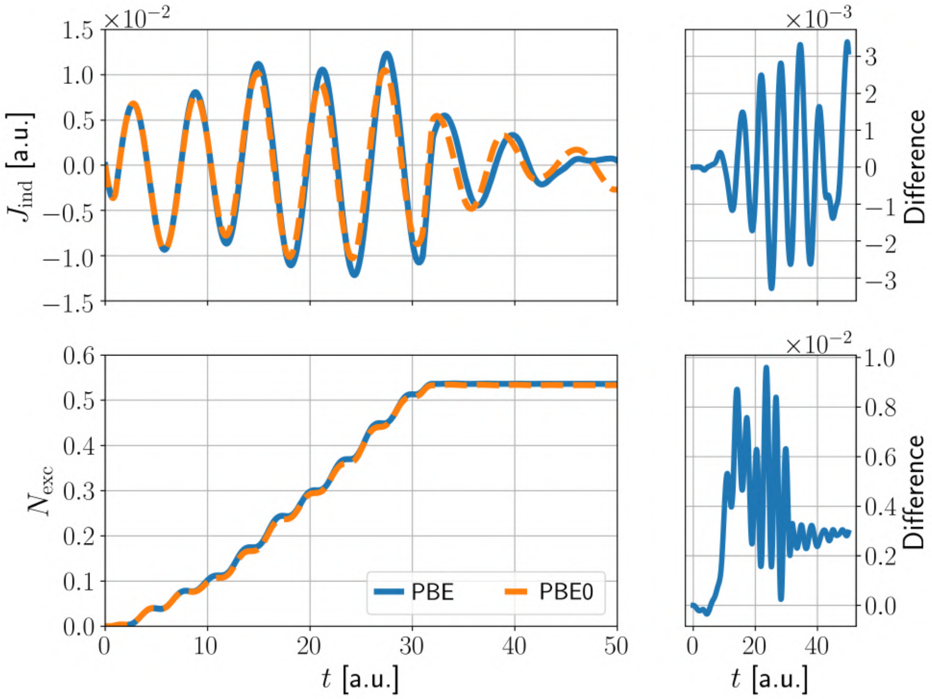

Figure 6: Comparison of J_{ind} and N_{exc} between calculations with the PBE and PBE0 functional for diamond.

4.1.4 HSE

Overall, the results from HSE06 and PBE0 are very similar. J_{ind} and N_{exc} differ of the order of 10^{-5}. For HSE, it can be investigated whether N_{exc} and J_{ind} resembles the values of PBE for larger values of ω. For this reason, calculations with different values for ω were performed. For the convergence parameters, `rgkmax`=5, Δt=0.05 a.u, N_{empty}=20 and 3x3x3 k points were chosen under the assumption that the convergence behavior would be similar to that of PBE0. For the N_{exc} depicted in Fig. 7, a similar behavior to the band gaps for different ω can be identified. The difference between the curves is small, but an increase in ω corresponds to a larger N_{exc}. This can be explained due to the band gaps. Interestingly, the curve for PBE follows $\omega = 1$ up to around 25 time steps to then approach the curve for $\omega = 0.3$. The PBE curve follows closely the HSE path one would predict from the GS energies at the beginning of the laser pulse. While the laser pulse progresses, the different time evolution of the systems becomes more dominant. J_{ind} for different ω is given in Fig. 8. When ω is increased, an increase for the minima and maxima can be observed while the laser is applied. After the laser is turned off, this trend seems to be reversed, except for $\omega = 1$. In this region, a larger ω corresponds to smaller minima. The curve for $\omega = 1$ shows similarities to the one calculated with PBE.

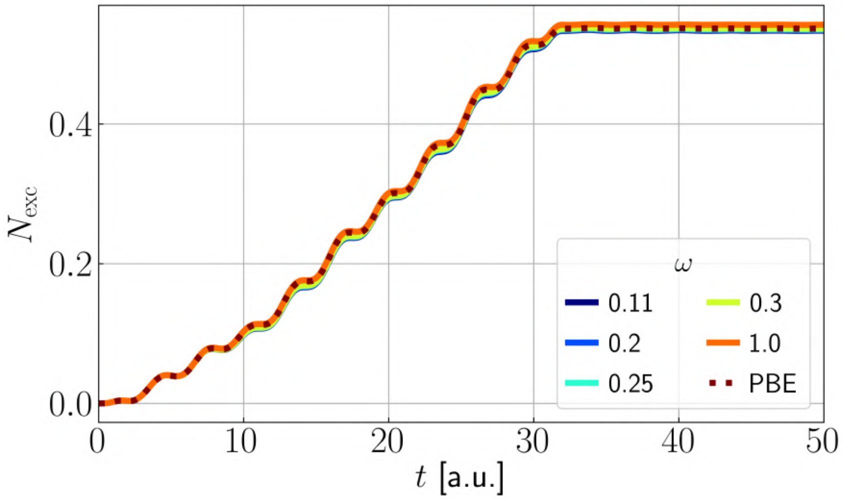

Figure 7: N_{exc} calculated with the HSE functional for different values of ω. The dotted line shows the N_{exc} for PBE.

4.1.5 Comparison with the octopus code

As a benchmark for the implementation of hybrid functionals in RT-TDDFT in `exciting`, we compare J_{ind} and N_{exc} with the results of the octopus code [31]. octopus is an ab initio code which employs a real-space mesh and pseudopotentials [31]. It has been used already to perform a comparison with `exciting` [2]. For the following octopus calculations, a real space grid with a spacing of 0.17 Å was found to give suitably converged results. The

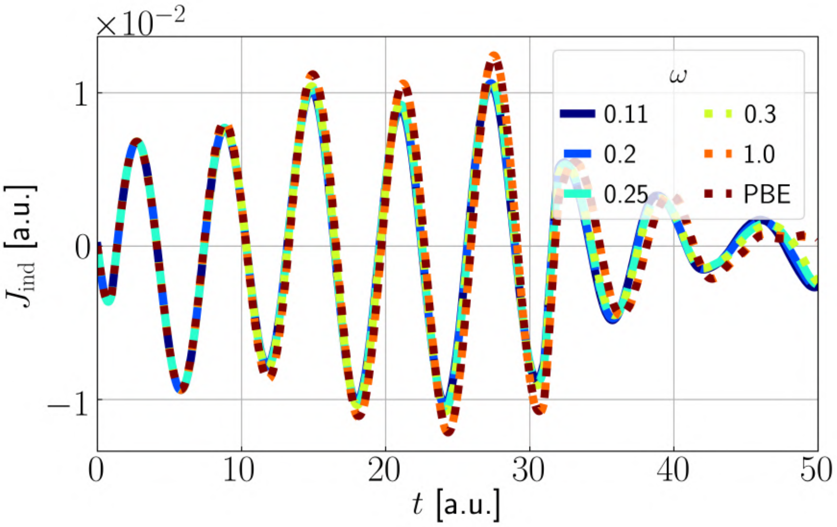

Figure 8: J_{ind} calculated with the HSE functional for different values of ω. Additionally, J_{ind} for PBE is shown (dotted line).

calculations with octopus were provided by Ronaldo Rodrigues Pelá.

First, we perform a comparison for the PBE functional. N_{exc} and J_{ind} obtained by `exciting` and octopus are given in Fig. 9. The difference between N_{exc} and J_{ind} is given on the right. The similarities between `exciting` and octopus is remarkable. The difference for N_{exc} and J_{ind} is two orders of magnitude smaller than the value itself. For N_{exc}, the magnitude of the difference rises over the course of the calculation until the laser is turned off. At the end of the calculation, `exciting` estimates a slightly lower number of N_{exc} than octopus. For J_{ind}, the difference of the curves, given on the right side of the plot, show their maxima and minima with a slight delay compared to the maxima and minima of J_{ind}.

The numerical comparison between `exciting` and octopus is limited by the differences between both codes introduced by the different basis set and core electron treatment. In order to evaluate thesmall differences between `exciting` and octopus, it is useful to investigate the impact of different pseudopotentials for octopus. To that end, Ronaldo Rodrigues Pelá performed additional octopus calculations with the standard octopus pseudopotential [31]. For the shown above comparison with `exciting`, the optimized norm conserving PBE pseudopotential (sg15) was used [32]. The comparison between sg15 and the standard pseudopotential is shown in Fig. 20 and 21 for PBE and PBE0

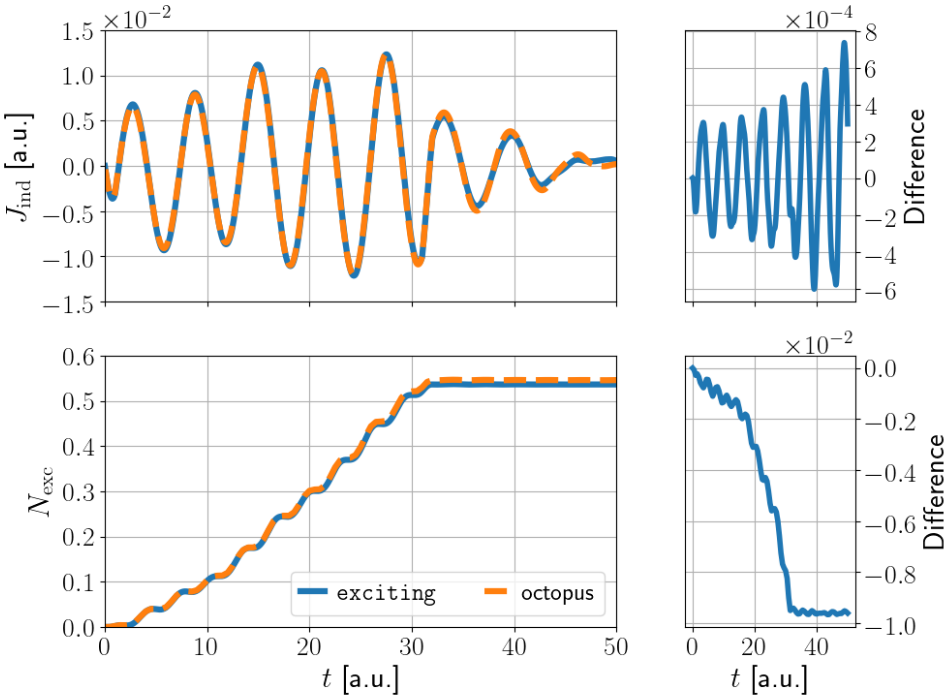

Figure 9: Comparison of J_{ind} and N_{exc} between `exciting` and octopus with PBE for diamond. The differences of the left curves are given on the right.

respecively. The difference between pseudopotentials is in the same order of magnitude or larger than between the `exciting` and octopus implementation.

For the hybrid functionals, the same comparison as above was performed. The comparison with octopus for HSE06 (Fig. 11) is very similar to the comparison with octopus for PBE0. For this reason, a special focus is put on PBE0 in the following section. For PBE0, N_{exc} and J_{ind} are given in Fig. 10 with the difference given on the right. Similarly to PBE, the agreement between both curves is remarkable and comparable to the differences for PBE. One exception is that difference of N_{exc} increases over time but does not become constant. The reason is that the N_{exc} for octopus does not become constant after the laser pulse is turned off. Overall, as for PBE, the difference is two orders of magnitude smaller than the value itself. This gives a high degree of confidence in the implementation.

However, the results for the non-local current can not be compared with octopus. The non-local current depends on the treatment of the core states as described in Sec. 3.2.2. For the shown PBE0 calculation of `exciting`, the non-local current is given in Fig. 12. It

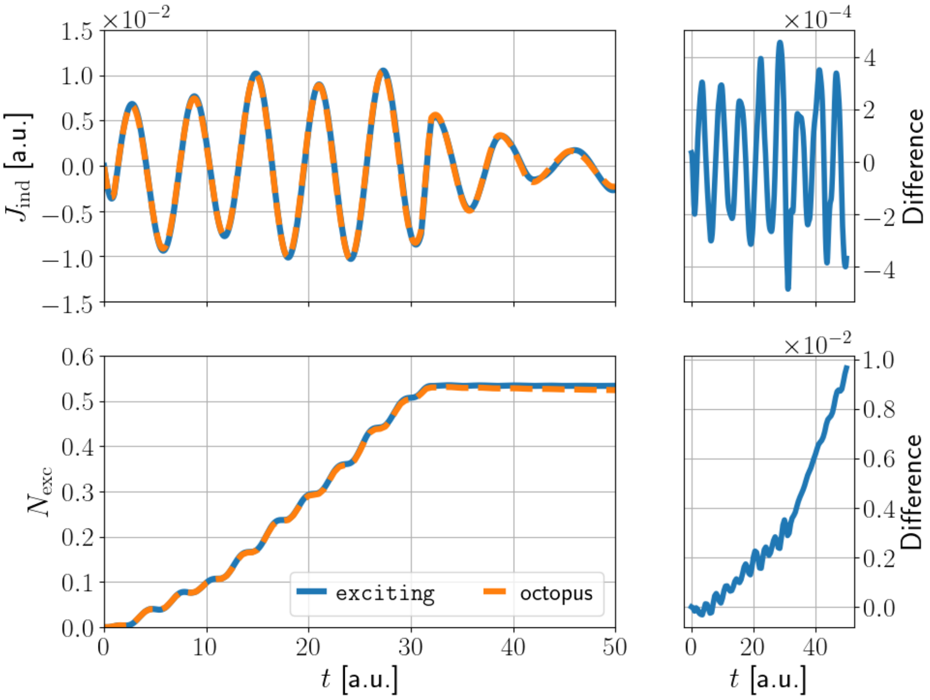

Figure 10: Comparison of J_{ind} and N_{exc} between `exciting` and octopus with PBE0 for diamond. The differences of the left curves are given on the right.

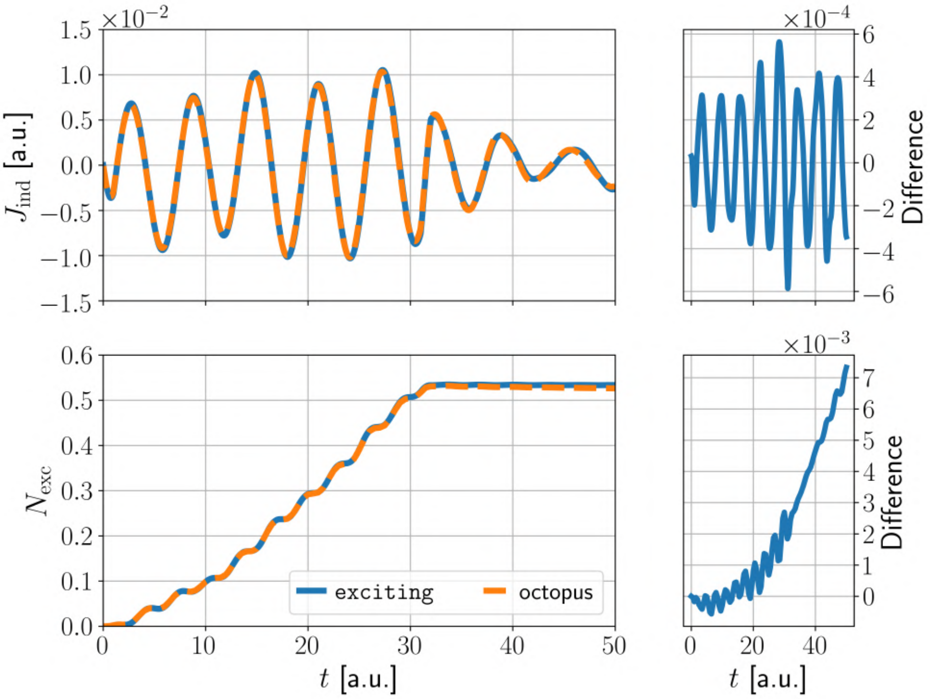

Figure 11: Comparison of J_{ind} and N_{exc} between `exciting` and octopus with HSE06 for diamond. The differences of the left curves are given on the right.

was found to be of the order of 10^{-5}. In Fig. 12, another calculation is depicted treating all electrons as valence, as opposed to using the default species file. As described in Sec. 3.2.2, when all electrons are treated as valence, J_{NL} includes two sums which cancel each other out, and the non-local current goes to zero. For the default species file, the maxima, and minima of J_{NL} are located at the positions where J_{ind} approaches zero while the laser is applied. To test the implementation of J_{NL}, the consistency check described in Sec. 3.2.2 was performed. The difference was of the order of 10^{-15}. This gives a high level of confidence in the implementation of $J_{\mathrm{NL}}(t)$. Overall, $J_{\mathrm{NL}}(t)$ has a vanishing impact on the overall current response.

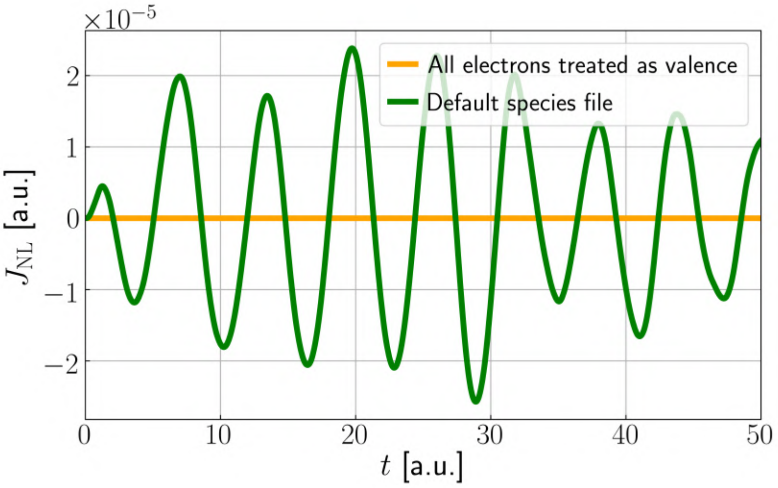

Figure 12: Non-local current of diamond with PBE0 obtained with different core electron treatment.

4.2 Boron nitride

Boron nitride (BN) has established itself as a synthetic alternative to diamond. Cubic BN shares similarities with diamond, both in bonding and physical properties and has an indirect gap of $E_\mathrm{g} = 6.2$ eV [33]. This material can be used to investigate the implementation with two different elements in the unit cell.

4.2.1 Computational details

The structure of BN was chosen in the face cubic centered configuration with a lattice constant of 3.4817 Å and the distance between boron and nitride as 1.5657 Å. Since the calculations were conducted with 64 k points, the (0.5 0 0.5) (X) point was probed and $E_{\Gamma-\mathrm{X}}$ can be seen as an approximation for the experimental band gap. As for diamond, convergence tests were conducted for `rgkmax` with PBE and PBE0 and N_empty with PBE0. The band gaps with respect to `rgkmax` are listed in Tab. 4 and with respect to N_empty in Tab. 5. For `rgkmax`$= 5$ and $N_\mathrm{empty} = 20$, the band gaps are converged up to 20 meV.

For the RT-TDDFT calculation, a laser pulse was applied along the [111] direction. The field takes the form of Eq. 4.1 with the envelope function:

$$f(t) = \sin^2(\pi(t - t_0)/T_\mathrm{pulse}). \tag{4.3}$$

The amplitude E_0 was chosen as 5.7735, the angular frequency ω as 1, the phase ϕ as 0, and the pulse duration T_pulse as 30, all given in a.u. The applied field is depicted in Fig.13. The dotted line shows the sinusoidal envelope function times the amplitude.

Table 4: Band gaps (in eV) of BN for different values of `rgkmax` obtained with the PBE and PBE0 functional. Listed are the eigenvalue differences from Γ to Γ and from Γ to X.

	$E_{\Gamma-\Gamma}$		$\mathrm{E}_{\Gamma-\mathrm{X}}$	
`rgkmax`	PBE	PBE0	PBE	PBE0
4	8.76	11.31	4.36	6.50
5	8.79	11.37	4.31	6.51
6	8.79	11.38	4.43	6.63

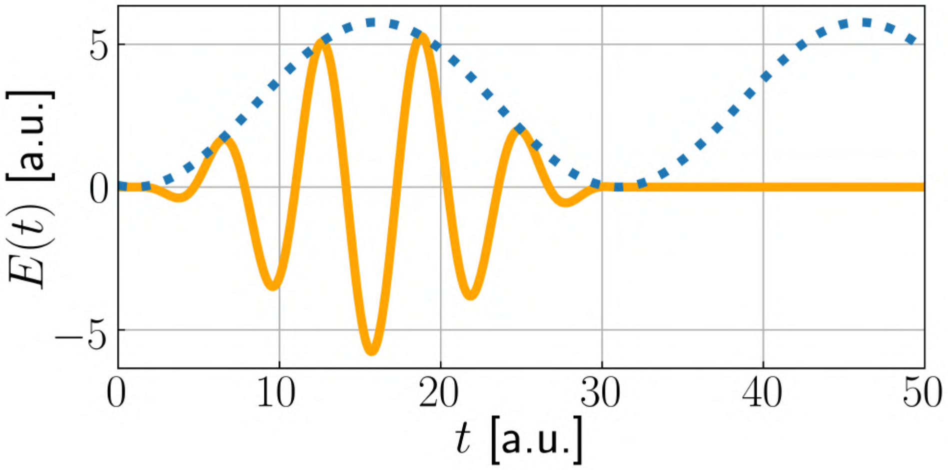

Figure 13: Laser pulse used for BN. The dotted line shows the envelope function times the amplitude.

Table 5: Band gaps (in eV) for different values of N_{empty}, calculated with the PBE0 functional.

N_{empty}	$E_{\Gamma-\Gamma}$	$E_{\Gamma-\text{X}}$
10	11.42	6.57
20	11.37	6.51
30	11.37	6.49
40	11.36	6.48

Table 6: Band gaps (in eV) for different ω, with PBE and PBE0. For these, `rgkmax`= 5 and $N_{\text{empty}} = 20$ was chosen.

ω	$E_{\Gamma-\Gamma}$	$E_{\Gamma-\text{X}}$
0.11	10.57	5.71
0.15	10.32	5.48
0.2	10.08	5.26
0.25	9.89	5.10
0.3	9.72	4.96
1	8.90	4.38
PBE	8.79	4.31
PBE0	11.37	6.51

4.2.2 Convergence test of RT-TDDFT with hybrids

As for diamond, the convergence behavior was investigated with respect to `rgkmax`, Δt, and N_{empty}. For these parameters, N_{exc} and J_{ind} were calculated with the PBE and PBE0 functional. For the other parameters, `rgkmax=5`, $\Delta t = 0.05$, and $N_{\text{empty}} = 20$ was used as a default.

Again, the convergence behavior of PBE, given in Appendix 6.3, is overall very similar to that of PBE0. The convergence of N_{exc} and J_{ind} with PBE0 with respect to `rgkmax` is given in Fig. 14. The RMSE decreases quickly with respect to `rgkmax`. A smaller number of `rgkmax` leads to a smaller value of the N_{exc}. In accordance to the difference of band gaps from `rgkmax`=4 to `rgkmax`=5, also the RMSE shows a notable difference. J_{ind} seems already quite converged to eyesight, with the most notable difference after the laser is turned off. In comparison to diamond, the convergence of J_{ind} seems faster. The data shows faster convergence with respect to `rgkmax` with PBE0 than with PBE shown in the Appendix (Fig. 23).

As with diamond, a quick convergence was found for Δt (not shown here). The convergence behavior for PBE0 was found almost identical to PBE.

The convergence of N_{exc} and J_{ind} with respect to N_{empty} are given in Fig. 15. N_{exc} converges swiftly in regard to N_{empty}. For $N_{\text{empty}} = 10$, N_{exc} does not remain constant, but decreases by 0.0011 after the laser is turned off. As mentioned, this suggests that the KS wave functions for occupied and unoccupied states do not form a complete set for this value of N_{empty}. As for diamond, J_{ind} becomes sensitive to N_{empty} with the use of the PBE0 functional. However, the convergence of J_{ind} is fast.

4.2.3 Comparison between PBE and PBE0

The comparison between J_{ind} and N_{exc} with PBE and PBE0 for `exciting` is given in Fig. 16. Interestingly, the curves show very little difference up 20 time steps. After that, J_{ind} with PBE0 is slightly larger than with PBE. It takes a rather different form after the laser is turned off. N_{exc} takes as a smaller value with PBE than PBE0 after the laser is turned off. This is counterintuitive to the band gaps of PBE and PBE0 and suggests that

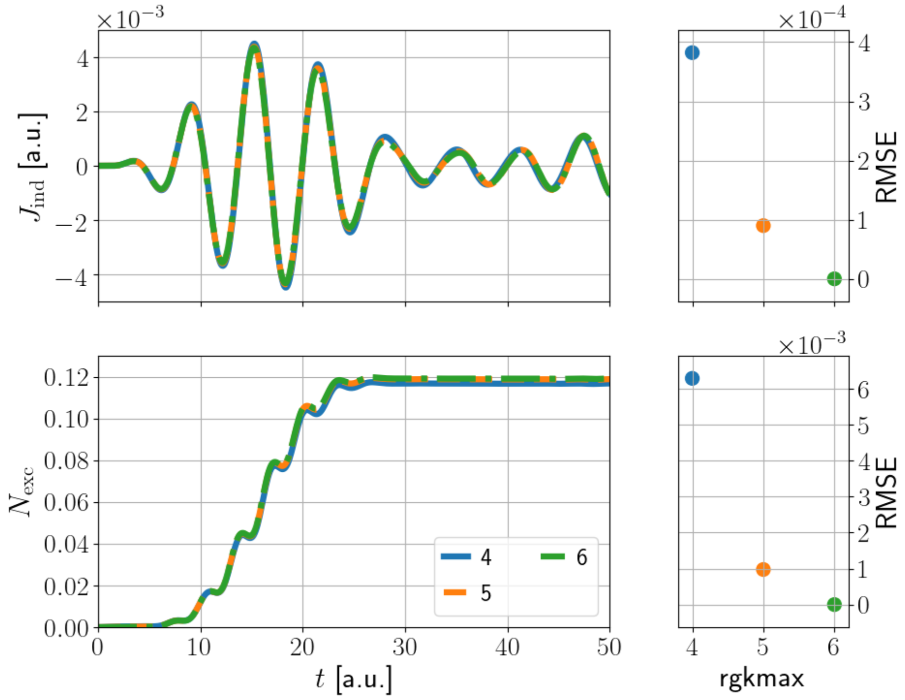

Figure 14: Convergence behavior of J_{ind} and N_{exc} with respect to `rgkmax`. The used functional was PBE0. `rgkmax`$=6$ was used as reference.

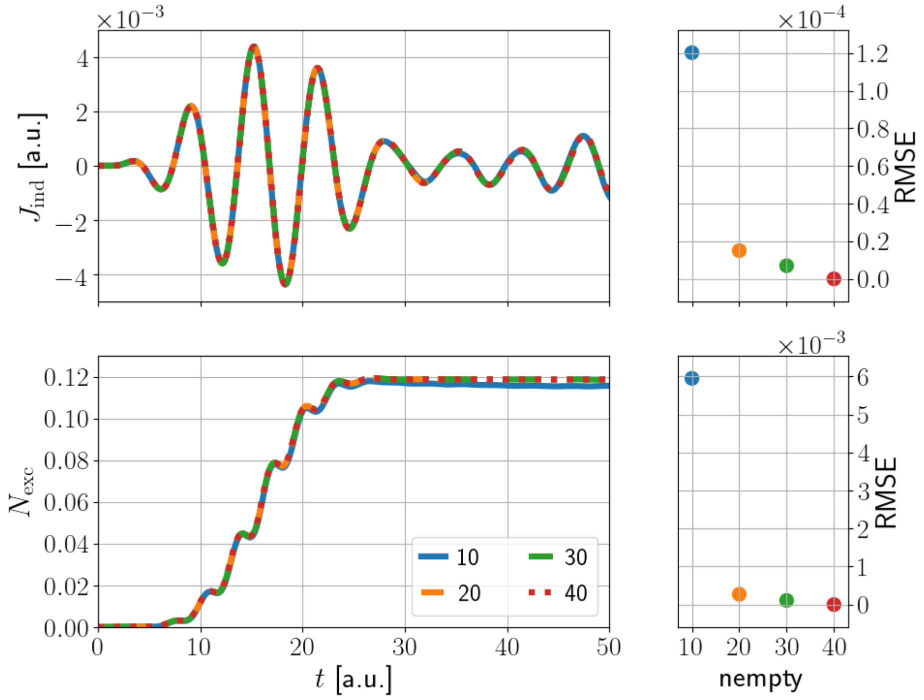

Figure 15: Convergence behavior of J_{ind} and N_{exc} with respect to N_{empty}. $N_{\mathrm{empty}} = 40$ was used as reference.

the evolution at the end of the laser pulse is not dominated by the GS properties for BN.

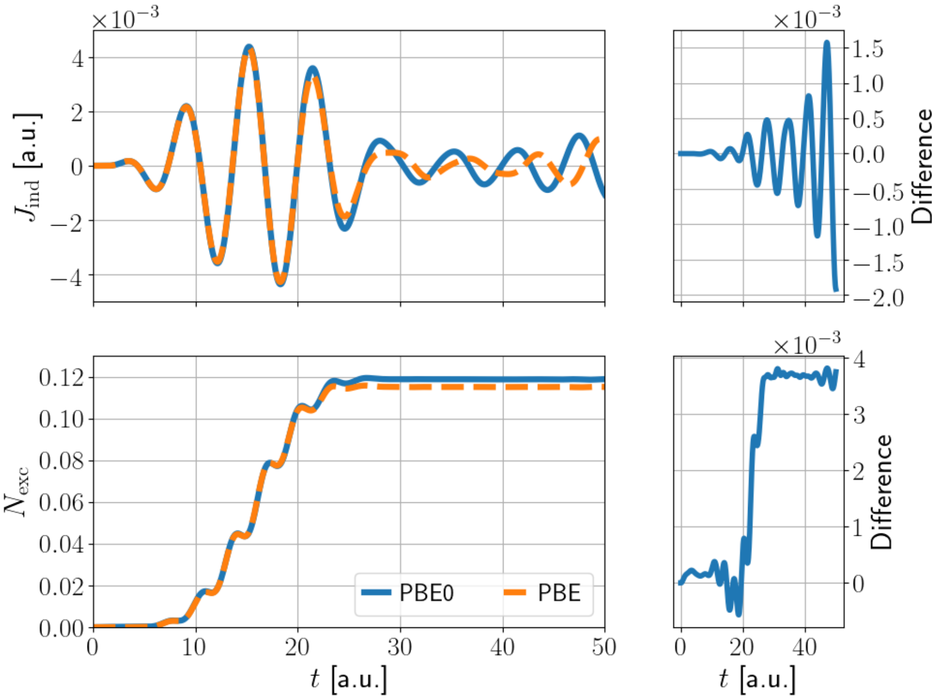

Figure 16: Comparison of J_{ind} and N_{exc} between calculations with the PBE and PBE0 functional for BN. The differences of the left curves are given on the right.

4.2.4 Comparison with the octopus code

Analogous to diamond, a comparison with the octopus code was conducted. The comparison between octopus and `exciting` with PBE is given in Fig. 17. The results are in very good agreement with each other with a difference one order of magnitude smaller than the value itself. J_{ind} from octopus is slightly smaller than J_{ind} from `exciting` while the laser is applied, and a larger value after the laser is turned off. N_{exc} is in good agreement between `exciting` and octopus.

For PBE0, the comparison is given in Fig. 18. The difference in J_{ind} behaves similar to that of J_{ind} in PBE. However, the value of N_{exc} with `exciting` is slightly smaller than the value of octopus. In contrast to PBE, N_{exc} from octopus does not remain constant after the laser is turned off. This leads to a steadily increasing difference. However, both curves are in good agreement overall. This gives a high degree of confidence in the implementation, as it was tested favorably with two elements in the unit cell against the results of octopus.

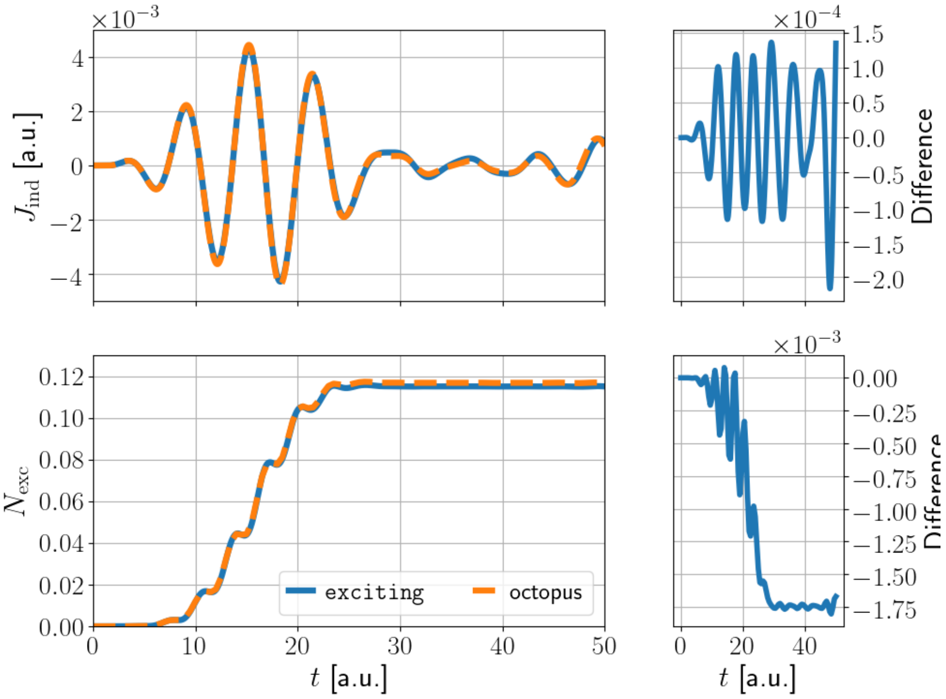

Figure 17: Comparison between `exciting` and octopus calculations with PBE functionals. The differences of the left curves are given on the right.

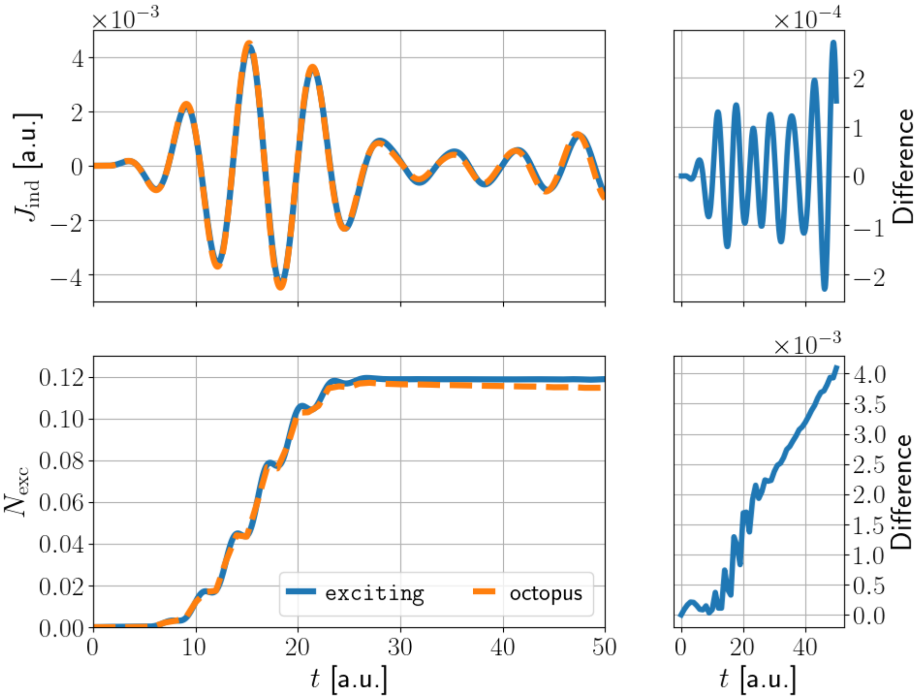

Figure 18: Comparison between `exciting` and octopus calculations with PBE0 functionals. The differences of the left curves are given on the right.

5 Conclusions and outlook

In this work, the implementation of hybrid functionals for RT-TDDFT in `exciting` was presented. The implementation included the incorporation of the already implemented non-local potential into the time-dependent framework. Furthermore, a new term, the non-local current, was introduced into RT-TDDFT. The non-local current was identified as an artifact, which had a vanishing impact on the overall current response for diamond and boron nitride. However, the behavior of the non-local current for more complicated materials remains to be analyzed.

RT-TDDFT calculations with hybrids, especially with a dense k point grid, can be very costly. Thus, an open challenge is to increase the speed of the calculation. This can be accomplished by full OMP/MPI support. Another method that can be considered is to update the non-local potential and non-local current not every time step, but after an integer interval of time steps.

The implementation was successfully tested for diamond and boron nitride, which, given together, provides a high level of confidence in its correctness. This implementation opens the path to simulate materials with more accuracy. In the future, the dielectric and optical conductivity tensor from RT-TDDFT can be investigated using a hybrid functional. This is an essential building block to study exciton dynamics.

6 Appendix

6.1 Derivation of the fourier transform

The Fourier transform $\boldsymbol{F}^{\boldsymbol{q}}_{\boldsymbol{G}}$ is given by:

$$\boldsymbol{F}^{\boldsymbol{q}}_{\boldsymbol{G}} = \int\int e^{-\mathrm{i}(\boldsymbol{q}+\boldsymbol{G})\boldsymbol{r}} \boldsymbol{F}(\boldsymbol{r},\boldsymbol{r}') e^{\mathrm{i}(\boldsymbol{q}+\boldsymbol{G})\boldsymbol{r}'} \boldsymbol{r} d\boldsymbol{r}', \tag{6.1}$$

where $\boldsymbol{F}(\boldsymbol{r},\boldsymbol{r}') = \frac{\boldsymbol{r}-\boldsymbol{r}'}{|\boldsymbol{r}-\boldsymbol{r}'|}$ for PBE0 and $\boldsymbol{F}(\boldsymbol{r},\boldsymbol{r}') = \frac{\mathrm{erfc}(\omega(\boldsymbol{r}-\boldsymbol{r}'))}{|\boldsymbol{r}-\boldsymbol{r}'|}$ for HSE06. In the following, we make the derivation for HSE06. The integrals can be taken over the unit cell with the volume V with the crystal volume Ω:

$$\boldsymbol{F}^{\boldsymbol{q}}_{\boldsymbol{G}} = \frac{\Omega}{V}\int_V\int_V e^{-\mathrm{i}(\boldsymbol{q}+\boldsymbol{G})\boldsymbol{r}} \boldsymbol{F}(\boldsymbol{r},\boldsymbol{r}') e^{\mathrm{i}(\boldsymbol{q}+\boldsymbol{G})\boldsymbol{r}'} \boldsymbol{r} d\boldsymbol{r}', \tag{6.2}$$

with a change of variable, the 2-dimensional integral can be reduced, defining $\boldsymbol{u} = \boldsymbol{r} - \boldsymbol{r}'$ and $\boldsymbol{q}' = \boldsymbol{q} + \boldsymbol{G}$, Eq. 6.2 becomes:

$$\boldsymbol{F}^{\boldsymbol{q}}_{\boldsymbol{G}} = \int_V \boldsymbol{F}(\boldsymbol{u}) e^{\mathrm{i}(\boldsymbol{q}')\cdot\boldsymbol{u}} d\boldsymbol{u}. \tag{6.3}$$

Another change of variable can be conducted in which:

$$\boldsymbol{u} = u(\sin\theta\cos\phi, \sin\theta\sin\phi, \cos\theta). \tag{6.4}$$

With that, we can point our coordinate axis in the direction of $\boldsymbol{q}$, and Eq. 6.3 becomes:

$$\boldsymbol{F}^{\boldsymbol{q}}_{\boldsymbol{G}} = \mathrm{lim}_{\sigma\rightarrow 0} 2\pi \int e^{-\mathrm{i}\cos\theta \boldsymbol{q}'\cdot\boldsymbol{u}} (0,0,\cos\theta) \frac{\mathrm{erf}(\omega u)\mathrm{e}^{-\sigma u}}{u} u^2 \sin\theta du d\theta. \tag{6.5}$$

This can be further reduced using the relation:

$$\int_0^\pi e^{\mathrm{i}\cos\theta \boldsymbol{q}'\cdot\boldsymbol{u}} \cos\theta\sin\theta d\theta = \frac{e^{\mathrm{i}q'u}(\mathrm{i}qu - 1) + e^{-\mathrm{i}q'u}(\mathrm{i}q'u + 1)}{q'^2u^2}. \tag{6.6}$$

With that, Eq. becomes:

$$\boldsymbol{F}^{\boldsymbol{q}}_{\boldsymbol{G}} = \mathrm{lim}_{\sigma\rightarrow 0} \frac{2\pi}{q'^2} \hat{q}' \int_0^\infty \mathrm{erf}(\omega u)\mathrm{e}^{-\sigma u}[e^{\mathrm{i}q'u}(\mathrm{i}q'u - 1) + e^{-\mathrm{i}q'u}(\mathrm{i}q'u + 1)]du. \tag{6.7}$$

The terms of this equation can be evaluated separately:

$$\mathrm{lim}_{\sigma\rightarrow 0} \int_0^\infty \mathrm{erf}(\omega u)\mathrm{e}^{-\sigma u}[-e^{\mathrm{i}q'u} + e^{-\mathrm{i}q'u}]du = -\frac{2\mathrm{i}}{q'}\big(1 - \mathrm{e}^{\frac{-q'^2}{4\omega^2}}\big) \tag{6.8}$$

$$\mathrm{lim}_{\sigma\rightarrow 0} \int_0^\infty \mathrm{erf}(\omega u)\mathrm{e}^{-\sigma u}[\mathrm{i}q'u(e^{\mathrm{i}q'u} + e^{-\mathrm{i}q'u})]du = \frac{\mathrm{i}}{q'\omega^2}\big(\mathrm{e}^{\frac{-q'^2}{4\omega^2}}(q'^2 + 2\omega^2) - 2\omega^2\big) \tag{6.9}$$

The whole expression becomes:

$$\boldsymbol{F}_{\boldsymbol{G}}^{\boldsymbol{q}} = \frac{8\pi \mathrm{i}\boldsymbol{q}'}{q'^4}\Bigg(-1 + \mathrm{e}^{\frac{-q'^2}{4\omega^2}}(1 + \frac{q'^2}{4\omega^2})\Bigg), \tag{6.10}$$

which goes to zero for $q' \rightarrow 0$. When we substitute $\boldsymbol{q}'$ we recover:

$$\boldsymbol{F}_{\boldsymbol{G}}^{\boldsymbol{q}} = \begin{cases} \frac{8\pi \mathrm{i}(\boldsymbol{q}+\boldsymbol{G})}{|\boldsymbol{q}+\boldsymbol{G}|^4}\Bigg[-1 + \exp\Big(\frac{-(\boldsymbol{q}+\boldsymbol{G})^2}{4\omega^2}\Big)\Big(1 + \frac{(\boldsymbol{q}+\boldsymbol{G})^2}{4\omega^2}\Big)\Bigg], & \boldsymbol{q}+\boldsymbol{G} \neq 0 \\ \boldsymbol{0}, & \boldsymbol{q}+\boldsymbol{G} = 0, \end{cases}$$

6.2 Supporting graphics for diamond

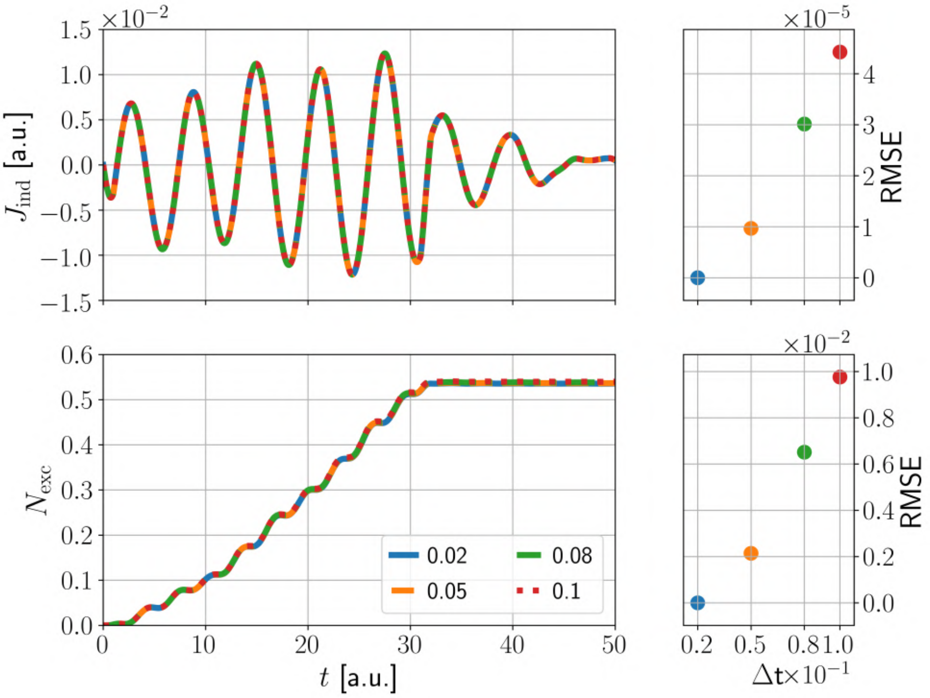

Figure 19: Convergence behavior of J_{ind} and N_{exc} with respect to the time step for diamond. The used functional was PBE0. $\Delta t = 0.02$ was used as reference.

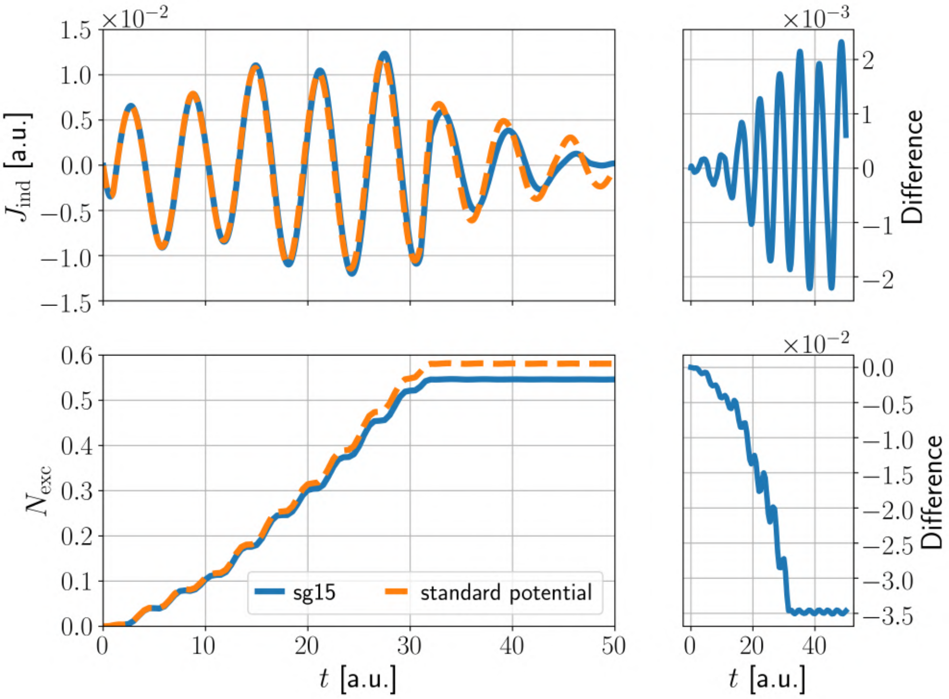

Figure 20: Comparison between the sg15 and the standard pseudopotential with PBE from octopus.

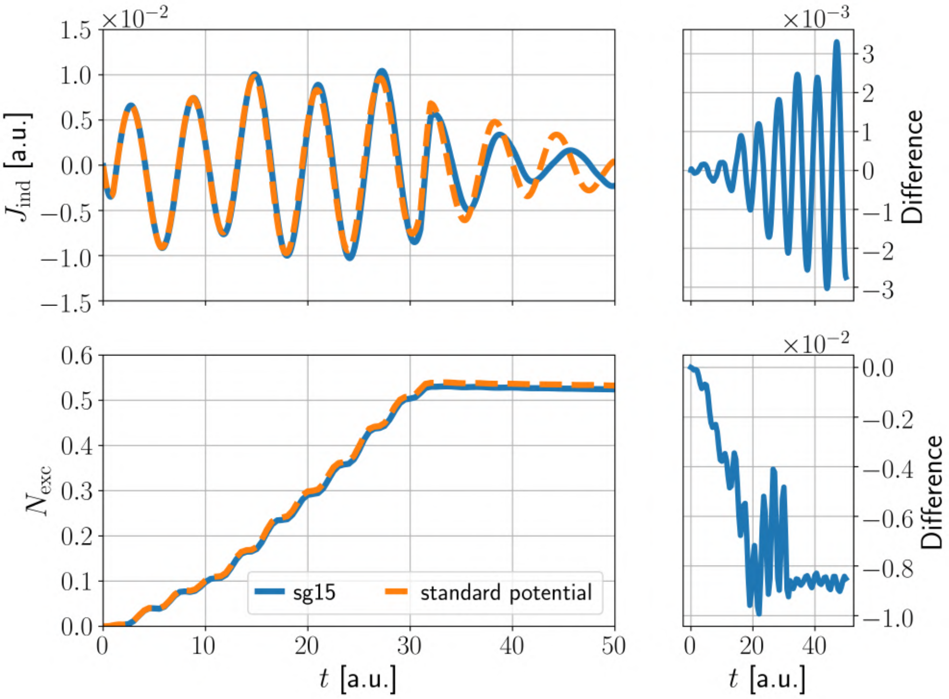

Figure 21: Comparison between the sg15 and the standard pseudopotential with PBE0 from octopus.

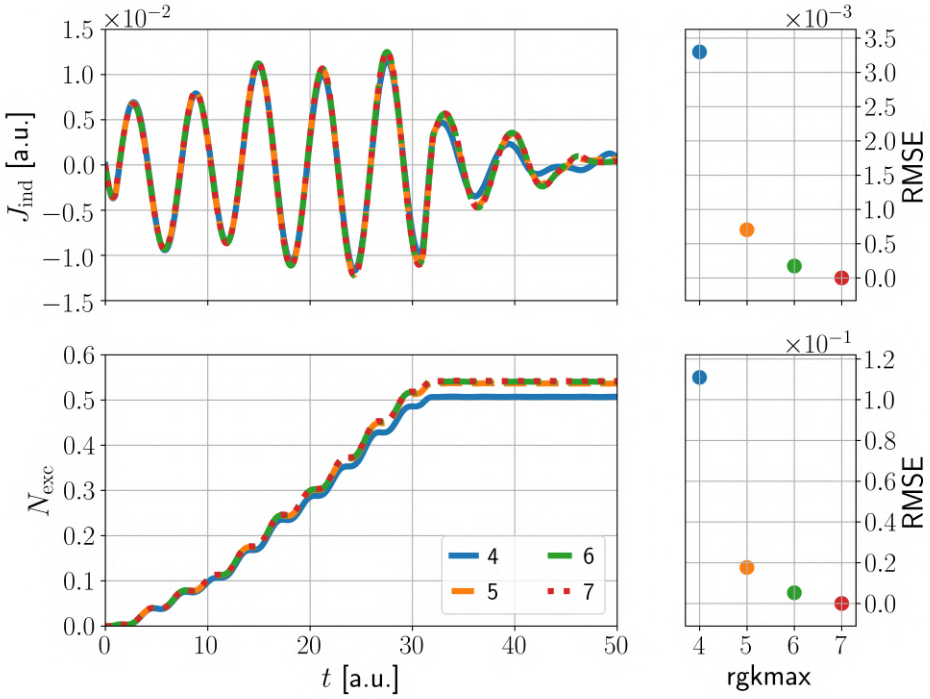

Figure 22: Convergence behavior of J_{ind} and N_{exc} with respect to the time step for diamond. The used functional was PBE. `rgkmax`= 7 was used as reference.

6.3 Supporting graphics for boron nitride

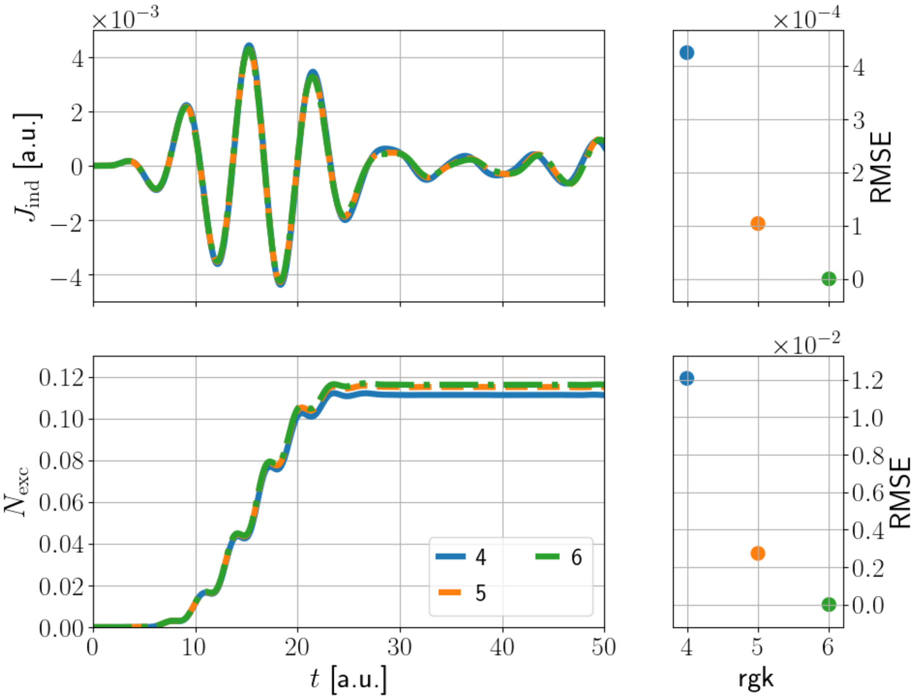

Figure 23: Convergence behavior of J_{ind} and N_{exc} with respect to `rgkmax` for boron nitride. The used functional was PBE. `rgkmax`= 6 was used as reference.

References

[1] A. Gulans, S. Kontur, C. Meisenbichler, D. Nabok, P. Pavone, S. Rigamonti, S. Sagmeister, U. Werner, and C. Draxl, Journal of Physics: Condensed Matter **26**, 363202 (2014).

[2] R. R. Pela and C. Draxl, Electronic Structure **3**, 037001 (2021).

[3] P. Hohenberg and W. Kohn, Physical review **136**, B864 (1964).

[4] W. Kohn and L. J. Sham, Phys. Rev. **140**, A1133 (1965).

[5] C. A. U. Miguel A.L. Marques, Time-Dependent Density Functional Theory (Springer-Verlag Berlin, 2006).

[6] K. Burke and L. O. Wagner, International Journal of Quantum Chemistry **113**, 96 (2013), https://onlinelibrary.wiley.com/doi/pdf/10.1002/qua.24259 .

[7] P. Morgante and R. Peverati, International Journal of Quantum Chemistry **120**, e26332 (2020), https://onlinelibrary.wiley.com/doi/pdf/10.1002/qua.26332 .

[8] R. M. Martin, "Functionals for exchange and correlation ii," in Electronic Structure: Basic Theory and Practical Methods (Cambridge University Press, 2020) p. 188–214, 2nd ed.

[9] R. M. Martin, "Functionals for exchange and correlation i," in Electronic Structure: Basic Theory and Practical Methods (Cambridge University Press, 2020) p. 171–187, 2nd ed.

[10] J. P. Perdew, K. Burke, and M. Ernzerhof, Phys. Rev. Lett. **77**, 3865 (1996).

[11] P. Borlido, T. Aull, A. W. Huran, F. Tran, M. A. L. Marques, and S. Botti, Journal of Chemical Theory and Computation **15**, 5069 (2019), pMID: 31306006, https://doi.org/10.1021/acs.jctc.9b00322 .

[12] A. Seidl, A. Görling, P. Vogl, J. A. Majewski, and M. Levy, Phys. Rev. B **53**, 3764 (1996).

[13] R. M. Martin, L. Reining, and D. M. Ceperley, "Mean fields and auxiliary sys-

tems," in Interacting Electrons: Theory and Computational Approaches (Cambridge University Press, 2016) p. 59–83.

[14] R. M. Martin, "Overview," in Electronic Structure: Basic Theory and Practical Methods (Cambridge University Press, 2020) p. 16–59, 2nd ed.

[15] A. I. Blair, A. Kroukis, and N. I. Gidopoulos, The Journal of Chemical Physics **142**, 084116 (2015), https://doi.org/10.1063/1.4909519 .

[16] R. M. Martin, "Uniform electron gas and sp-bonded metals," in Electronic Structure: Basic Theory and Practical Methods (Cambridge University Press, 2020) p. 110–127, 2nd ed.

[17] P. Borlido, J. Schmidt, A. Huran, F. Tran, M. Marques, and S. Botti, npj Computational Materials **6** (2020), 10.1038/s41524-020-00360-0.

[18] M. Betzinger, C. Friedrich, and S. Blugel, Physical Review B **81**, 195117 (2010).

[19] J. P. Perdew, M. Ernzerhof, and K. Burke, The Journal of Chemical Physics **105**, 9982 (1996), https://doi.org/10.1063/1.472933 .

[20] J. Heyd, G. E. Scuseria, and M. Ernzerhof, The Journal of Chemical Physics **118**, 8207 (2003), https://doi.org/10.1063/1.1564060 .

[21] A. V. Krukau, O. A. Vydrov, A. F. Izmaylov, and G. E. Scuseria, The Journal of Chemical Physics **125**, 224106 (2006), https://doi.org/10.1063/1.2404663 .

[22] M. A. L. Marques, J. Vidal, M. J. T. Oliveira, L. Reining, and S. Botti, Phys. Rev. B **83**, 035119 (2011).

[23] E. Runge and E. K. U. Gross, Phys. Rev. Lett. **52**, 997 (1984).

[24] J. I. Fuks, L. Lacombe, S. E. B. Nielsen, and N. T. Maitra, Physical chemistry chemical physics **20 41**, 26145 (2018).

[25] L. O. Wagner, Z.-h. Yang, and K. Burke, "Exact conditions and their relevance in tddft," in Fundamentals of Time-Dependent Density Functional Theory, edited by M. A. Marques, N. T. Maitra, F. M. Nogueira, E. Gross, and A. Rubio (Springer Berlin Heidelberg, Berlin, Heidelberg, 2012) pp. 101–123.

[26] A. Castro, M. A. L. Marques, and A. Rubio, The Journal of Chemical Physics **121**, 3425 (2004), https://doi.org/10.1063/1.1774980 .

[27] C. Friedrich, A. Gierlich, S. Blügel, and A. Schindlmayr, (2010).

[28] C. Friedrich, A. Schindlmayr, and S. Blügel, Computer Physics Communications **180**, 347 (2009).

[29] H. Jiang, R. I. Gómez-Abal, X.-Z. Li, C. Meisenbichler, C. Ambrosch-Draxl, and M. Scheffler, Computer Physics Communications **184**, 348 (2013).

[30] C. D. Clark, P. J. Dean, and P. V. Harris, Proceedings of the Royal Society of London. Series A, Mathematical and Physical Sciences **277**, 312 (1964).

[31] N. Tancogne-Dejean and M. J. T. e. a. Oliveira, The Journal of Chemical Physics **152**, 124119 (2020), https://doi.org/10.1063/1.5142502 .

[32] M. Schlipf and F. Gygi, Computer Physics Communications **196**, 36 (2015).

[33] M. Levinshtein, S. Rumyantsev, and M. S. Shur (2001).

Selbstständigkeitserklärung

Ich erkläre hiermit, dass ich die vorliegende Arbeit selbstständig verfasst und noch nicht für andere Prüfungen eingereicht habe. Sämtliche Quellen einschließlich Internetquellen, die unverändert oder abgewandelt wiedergegeben werden, insbesondere Quellen für Texte, Grafiken, Tabellen und Bilder, sind als solche kenntlich gemacht. Mir ist bekannt, dass bei Verstößen gegen diese Grundsätze ein Verfahren wegen Täuschungsversuchs bzw. Täuschung eingeleitet wird.

Berlin, 23.2.23,